Influence of high marine Ca/SO_4 ratio on alteration of submarine basalts at 2.41 Ga documented by triple O and Sr isotopes of epidote

Zakharov DO[1,2], Lundstrom CC[3], Laurent O[4,5], Reed MH[2], and Bindeman IN[2]

1- Institute of Earth Sciences, University of Lausanne, Lausanne, Switzerland 1015
2- Earth Sciences Department, 1272 University of Oregon, Eugene, OR USA 97402
3- Department of Geology, University of Illinois, 3081 Natural History Bldg, 1301 W Green Street, Urbana, IL USA 61801
4- Department of Earth Sciences, Institute for Geochemistry and Petrology, ETH Zürich, Clausiusstrasse, 25, Zürich, Switzerland 8092
5- CNRS, Géosciences Environnement Toulouse, Observatoire Midi-Pyrénées 14, Avenue Édouard Belin, Toulouse, France 31400

Corresponding author: David Zakharov david.zakharov@unil.ch

ABSTRACT

Over the course of Earth's history, marine sulfate concentrations have been increasing in response to long-term atmospheric oxygenation. In contrast to modern oceans, where abundant sulfate precipitates in hot oceanic crust as anhydrite, Precambrian oceans contained much less (~0-10 mM) sulfate, so that submarine hydrothermal systems were comparatively poor in anhydrite. As a step towards exploring the role of chemical evolution of seawater solutes, we investigate the reaction between basalt and seawater that took place at the ca. 2.43-2.41 Ga Vetreny Belt (Karelia craton, NW Russia) using fluid inclusion and multi-isotope measurements complemented by reactive transport and static aqueous-mineral equilibrium calculations. Using fluid inclusion measurements by LA-ICP-MS, we constrain the Sr concentration in the least modified fluids at the and address the effect of phase separation. Then, we complement the previous $\delta^{18}O - \Delta'^{17}O$ datasets with new $^{87}Sr/^{86}Sr$ measurements performed on ancient epidote from the Vetreny Belt and modern (0-6 Ma) oceanic epidote from Reykjanes, Iceland and the drilling site 504B in the eastern Pacific Ocean. The ancient epidote with $^{87}Sr/^{86}Sr_{initial}$ of 0.7029-0.7041 and $\Delta'^{17}O$ of –0.06 to 0.00 ‰ is best explained by a relatively high fraction (~90%) of marine Sr that was delivered from contemporaneous seawater without significant removal by early anhydrite. Using Monte-Carlo simulation of a dual-porosity model, we constrain the range of possible exchange trajectories based on the variability of physical parameters (porosity, fluid flow velocity, fracture spacing, recrystallization rates). Further, we use a series of static equilibrium seawater-basalt reaction calculations with emphasis on the possible range of Ca/SO_4 values at 2.41 Ga. Our calculations demonstrate that co-existing quartz and epidote in absence of feldspars represent equilibrium with less-evolved hydrothermal fluids. Consequently, equilibrium assemblage of quartz and epidote provide an insightful archive for marine Sr. High Ca/SO_4 ratio of seawater (>>1) and low concentration of anhydrite in submarine systems of the contemporaneous oceans promote a higher fraction of seawater Sr to be permanently stored in silicates of altered oceanic crust, while modern altered oceanic crust is depleted in radiogenic Sr due to partitioning into anhydrite, which partly returns into the ocean upon cooling.

Keywords: triple oxygen isotopes, marine sulfate, altered oceanic crust, epidote, mineral-aqueous equilibrium modeling

1. INTRODUCTION

Over time scales exceeding 10 Ma, the composition of the Earth's oceans is modulated by delivery and removal of major elements. Driven by exchange reactions with oceanic crust, hydrothermal circulation of seawater serves both as a sink and a source in budgets of many major elements. The composition of exchanged fluids released at submarine vents (i.e. black smokers) is considered to be rock-buffered with limited influence of seawater dissolved load (e.g. Berndt et al. 1989). However, the long-term changes of seawater concentrations driven by other factors such as continental weathering can modify the pathways that marine elements undergo during reactive transport within oceanic crust (Kump and Seyfried, 2005; Antonelli et al., 2017). In turn, the chemical signature acquired by altered oceanic crust is translated into the composition of fluids released at subduction zones. On billion-year timescale, one of the most prominent changes that affected seawater composition is the rise of sulfate. The overall rise of atmospheric pO_2 levels over geological time promoted an increase in oxidized marine species, particularly sulfate, which is intimately tied to the increasing oxidative capacity of terrestrial sulfide weathering (Holland, 1984; Canfield, 1998; Farquhar and Wing, 2003; Kah et al., 2004).

While chemical transfer between seawater and mid-ocean ridge basalts establishes a first-order control on the composition of the terrestrial ocean, the effect of secular rise of marine sulfate on alteration of oceanic crust is still poorly understood. In this contribution we focus on the effect of anhydrite precipitation during reactive circulation of seawater within hot oceanic crust. The high sulfate concentration of modern seawater causes precipitation of anhydrite ($CaSO_4$) during early stages of seawater-basalt reactions, distributing seawater-derived Ca and S in the upper section of altered oceanic crust (Fig. 1; Mills et al., 1998; Teagle et al., 1998). Consequently, the fluids that reach high-temperature alteration zones of oceanic crust are depleted in marine sources of these elements.

Strontium is an element geochemically similar to Ca and is commonly found in anhydrite in trace amounts (e.g. Teagle et al., 1998). Thus, the origin of elements incorporated in the

budgets of hydrothermal fluids and altered oceanic crust can be traced by Sr isotope compositions that ranges from ^{87}Sr-enriched modern seawater ($^{87}Sr/^{86}Sr$ = ~0.7092) to ^{87}Sr-depleted modern oceanic basalts ($^{87}Sr/^{86}Sr$ = 0.702-0.703). This Sr isotope distinction is commonly used to trace seawater-derived fluxes based on measurements of submarine vent fluids and altered rocks (e.g. Bickle and Teagle 1992; Alexander et al. 1993; Gillis et al. 2005; Turchyn et al. 2013). In addition, the $^{87}Sr/^{86}Sr$ measured in epidote has also been used to indirectly trace saturation of fluids with anhydrite (Antonelli et al., 2017). For context, the marine Ca and SO_4 concentration estimates and the $^{87}Sr/^{86}Sr$ ratios of marine carbonates are shown in Fig. 2.

This idea of feedbacks between marine Ca, SO_4 and Sr concentrations has been explored previously for the Phanerozoic seawater using the submarine hydrothermal record (Coogan, 2009; Turchyn et al., 2013; Antonelli et al., 2017) for which both $^{87}Sr/^{86}Sr$ of seawater and major element solute concentrations are reconstructed. In particular, Antonelli et al. (2017) highlighted that the evolving marine Ca/SO_4 ratio governs the amount of marine Sr incorporated into anhydrite vs. silicates in the oceanic crust using the $^{87}Sr/^{86}Sr$ of oceanic epidotes (see Figs. 1 and 2). Similar to the present study, Turchyn et al. (2013) combined O and Sr isotope measurements from Cambrian, Ordovician and Cretaceous ophiolites, pointing out that the elevated $^{87}Sr/^{86}Sr$ values of epidotes formed when marine sulfate was around 10 mM, much lower than contemporaneous marine Ca concentrations. It is important to note that anhydrite itself is rarely preserved in relicts of ancient oceanic crust due to its high solubility in cold water (<150 °C). Thus, the high-temperature Sr-bearing silicates can be informative of the marine SO_4 and Ca concentrations. Compared to the Phanerozoic, it is obvious that in the Precambrian, before the first appearance of evaporitic sulfates at ~2.4-2.3 Ga (Schröder et al., 2008), low-sulfate seawater would result in anhydrite-poor submarine systems (Kump and Seyfried, 2005). However, evidence of this has not been studied using actual submarine altered rocks.

We further explore low sulfate seawater-basalt reactions that took place in the early Paleoproterozoic using the well-preserved 2.41 Ga hydrothermally altered basalts from the Vetreny Belt of the Baltic (Fennoscandian) Shield, Russia. Using the lithologies that reflect areas of voluminous seawater flow through the ancient hydrothermal system, we study the influence of low sulfate concentration on the isotope systematics of high temperature altered rocks. Given that the solute concentrations of contemporaneous seawater are not reliably known, we use the Sr isotope record of these rocks as an indirect reflection of the Ca/SO_4 ratio. However, unlike the marine sedimentary record, high-temperature alteration minerals that form within oceanic crust are not straightforward indicators of seawater composition due to the rock-buffered reactions. Thus, we acknowledge that hydrothermally altered rocks cannot compare in accuracy to the sedimentary record because they do not reflect marine solute concentrations directly. On the other hand, the isotope signals recorded in hydrothermally altered rocks may be more robust when compared to the sedimentary record due to the low solubility and chemical resilience of high-temperature silicates. Consequently, hydrothermally altered rocks can inform us of the pathways taken by elements during alteration of oceanic crust, a process that dominates concentration and isotope budgets of many elements. Below we outline the strategy to deconvolute the ancient seawater signature from altered rocks using fluid inclusion measurements, multi-isotope ratios and modeling approaches.

1.1 Fluid inclusion measurements combined with the $\delta^{18}O$—$\Delta'^{17}O$—$^{87}Sr/^{86}Sr$ approach

We apply fluid inclusion measurements, and multiple isotope ratios, $\delta^{17}O$, $\delta^{18}O$, and $^{87}Sr/^{86}Sr$, to constrain the isotopic signature of ancient hydrothermal fluids and initial seawater recorded within the alteration silicate minerals of submarine basalts. We specifically focus on the effect of precipitation of anhydrite, removal and delivery of marine Sr into the altered oceanic crust using a resilient Ca-silicate, epidote. Epidote forms in zones of focused upward flow at temperatures around 300 °C and is thought to reflect the marine Sr-pathways within altered oceanic crust (Alt et al., 1996; Gillis et al., 2005; Harris et al., 2015). Thus, we use fluid

inclusion elemental measurements to constrain the concentrations of Sr in ancient fluids and to recognize what processes could have affected the initial marine concentrations (i.e. phase separation). Further, we present several new $^{87}Sr/^{86}Sr$ measurements of the 2.41 Ga and recent (0-6 Ma) oceanic epidote. These relatively young epidotes were extracted from the 6 Ma altered oceanic crust drilled at the ODP site 504B in the eastern Pacific Ocean and from the modern geothermal system at Reykjanes, Iceland (boreholes RN12 and RN17B). These new Sr isotope measurements are then combined with the previously published triple O isotope values in the same samples (Zakharov and Bindeman, 2019; Zakharov et al., 2019b). We specifically target epidote's triple O isotope ratios because the small fractionation factor between the mineral and H_2O enables us to provide a close estimate of the O isotope ratio in the fluids. Traditionally used $\delta^{18}O$ value alone does not provide sufficient information on the isotope composition of the ancient fluids since both temperature and water-rock ratio affect the $\delta^{18}O$ value of epidote within ± 1 ‰ ($1000\ln\alpha_{epidote\text{-}water}$ between -1 and +1 at 300-400 °C; Matthews et al. 1983; Zheng 1993). Using the $\Delta'^{17}O$ values of epidote, defined as $10^3 \cdot \ln(\delta^{17}O \cdot 10^{-3} + 1) - 0.528 \cdot 10^3 \cdot \ln(\delta^{18}O \cdot 10^{-3} + 1)$, we rely on the O isotope fractionation between water and epidote, namely $\Delta'^{17}O_{water} - \Delta'^{17}O_{epidote}$ being minimal. Due to distinctly different O isotope compositions of mantle-derived rocks ($\delta^{18}O$ = ca. 6 ‰; $\Delta'^{17}O$ = -0.05 ± 0.01 ‰), seawater ($\delta^{18}O$ and $\Delta'^{17}O$ very close to 0 ‰) and meteoric waters (negative $\delta^{18}O$ and positive $\Delta'^{17}O$), epidote is a useful tracer of fluid-rock exchange reactions. Its $\Delta'^{17}O$ value must be very close to that of the fluids, within analytical uncertainty (i.e. ± 0.01 ‰), due to the relatively small mass-dependent fractionation at 300-400 °C (Hayles et al., 2018). This effect was demonstrated using the $\Delta'^{17}O$ measurements of geothermal fluids and co-existing epidote from modern hydrothermal systems of Iceland and altered oceanic crust (Zakharov et al., 2019b). Thus, the combined $\delta^{18}O$ – $\Delta'^{17}O$ – $^{87}Sr/^{86}Sr$ values of epidote allows us to directly trace the evolution of ancient submarine fluids without the need to correct for the temperature- or composition-dependent (i.e. epidote-clinozoisite; Matthews et al. 1983) fractionation. Further, due to the difference in concentrations of Sr and O contained in rocks and

fluids, the concomitant change in the $\delta^{18}O$ – $\Delta'^{17}O$ – $^{87}Sr/^{86}Sr$ values of epidote is then used to trace the reactive exchange between seawater and basalt. The shapes of the isotope exchange trajectories reflect the physical parameters of reactive seawater circulation (DePaolo and Getty, 1996; DePaolo, 2006) and can be used to constrain the Sr concentrations through geological time (Turchyn and DePaolo, 2019). We use two modeling approaches, static equilibrium and reactive transport, to narrow down the possible concentrations of marine Sr and the Ca/SO_4 ratio at 2.41 Ga.

1.2 Geological setting

The hydrothermally altered section of komatiitic basalts of the Vetreny Belt originated from the voluminous subaqueous eruption of high-Mg lavas (several km thick) during rifting of the Karelia craton, a part of the Baltic Shield (Puchtel et al., 1996, 1997, 2016; Zakharov and Bindeman, 2019; Kulikov et al., 2010; Mezhelovskaya et al., 2016). The summarized and simplified structure of the Vetreny Belt along with some representative sample photographs are shown in Figures 3 and 4. The overall stratigraphic context includes the lower part of the basin that is filled with early Paleoproterozoic (Sumian) sedimentary and volcano-sedimentary formations (Toksha, Kirichi, Kalgachi and Kozhozero suites) comprising sandstones, conglomerates, turbidites and dolostones (Kulikov et al., 2010). The upper part of the belt is composed of voluminous, several km-thick komatiities, komatiitic basalts and andesitic basalts that form differentiated flows and pillow lavas. Coeval mafic dikes and small intrusions cut the cratonic basement rocks and are also present within the volcanic rocks of the belt. One such intrusion named Ruiga is exposed in the northern part of the belt and is notably differentiated into peridotites and gabbros (see Fig. 4). In this study, we mainly focus on the seawater isotope signatures recorded in the hydrothermally altered varieties of the komatiitic basalts (Fig. 3). We also use samples of the sedimentary carbonates from the Kozhozero suite underlying the komatiitic basalts with the goal to capture the near-contemporaneous seawater isotope composition. This suite comprises marls, stromatolitic dolomites, marbles with micaceous shales

208 and sandstones (Mezhelovskaya et al., 2016). In this study we assume that these sedimentary
209 formations as well as the subaqueous pillow basalts reflect deposition in a shallow marine basin;
210 however the details of sedimentation setting are not well established. We further rely on other
211 contemporaneous basins of the Karelia craton and of the nearby Kola craton that have been
212 interpreted to record sedimentation in shallow marine or glacial-marine environment at ~2.4 Ga
213 (Ojakangas et al., 2001; Hanski and Melezhik, 2013).

214 The age of the komatiitic basalts is constrained by multiple geochronological studies. The
215 underlying Kirichi suite of andesites is dated to 2437 ± 3 Ma by high-precision isotope dilution
216 thermal ionization mass spectrometry (ID-TIMS) zircon measurements (Puchtel et al., 1997). We
217 consider this to be the maximum age of the Kozhozero sedimentary rocks that include the
218 carbonate unit analyzed for this study. The minimum age for the komatiitic basalts is constrained
219 by the precise 2407± 6 Ma Re-Os isochron for whole-rock samples, olivine and chromite
220 separates (Puchtel et al., 2016). Using ID-TIMS, a single zircon extracted from a differentiated
221 komatiitic basalt flow yielded the age of 2405 ± 6 Ma (Mezhelovskaya et al., 2016). The
222 subvolcanic intrusions are likely of similar age, as indicated by a Sm-Nd isochron measured in
223 the Ruiga intrusion (2390 ± 50 Ma; Kulikov et al., 2008) and by the upper intercept produced by
224 measurements of three discordant zircons (2415 ± 15 Ma; Mezhelovskaya et al., 2016). Thus, the
225 komatiitic basalts are 2.41 Ga, while together with the carbonates of the Kozhozero suite they are
226 constrained to between 2.43 and 2.41 Ga.

227 The preservation of the Vetreny Belt komatiitic basalt has been demonstrated previously
228 with geochemical investigations of unaltered volcanic glass, olivine phenocrysts and pristine
229 spinifex textures (Puchtel et al., 1996, 2001, 1997, 2016). The hydrothermally altered section of
230 the Vetreny Belt is also exceptionally well-preserved as demonstrated by presence of
231 undeformed pillow structures, delicate alteration of hyaloclastites and pillow rinds with original
232 textures, and by internally consistent quartz-epidote O isotope and fluid inclusion thermometry
233 (Zakharov and Bindeman, 2019). The epidotes measured for $^{87}Sr/^{86}Sr$ are the same as in the

studies of Zakharov and Bindeman (2019) and Zakharov et al. (2019), encompassing samples from the Vetreny Belt and recent altered oceanic crust. New bulk rock measurements of the Vetreny Belt formations are from: a) altered section of Ruiga intrusion used for conventional $\delta^{18}O$ values; b) the Lava Lake flow, a locality near Lev Gora containing least-altered basaltic rocks (see Fig.4) used for conventional $\delta^{18}O$ and $^{87}Sr/^{86}Sr$ values (sample description in Puchtel et al. 1996); c) underlying carbonates of the Kozhozero suite used for $\delta^{13}C$, $\delta^{18}O$, $^{87}Sr/^{86}Sr$. This wide range of samples is used to trace the contribution of marine isotope signals for both O and Sr, following the scheme introduced in the Section 1.1.

1.3 The record of marine sulfate in the early Paleoproterozoic

Since the ultimate purpose of this study is to assess anhydrite saturation in hydrothermal fluids as a consequence of evolving marine solutes, we must first review the current state of marine sulfate reconstructions for the Precambrian. We focus particularly on the early Paleoproterozoic, a period of dynamic change in atmospheric chemistry and sulfate concentrations. Modern oceans contain 28 mM sulfate, ~8 % of the total dissolved load (Berner and Berner, 1996), while the Phanerozoic (0.54 Ga to now) concentrations oscillated between 10 and 30 mM (see recent review Turchyn and DePaolo, 2019). This contrasts with the marine sulfate levels before the initiation of oxidative weathering at ~2.43- 2.42 Ga (Gumsley et al., 2017; Warke et al., 2020). Before this transition, termed the Great Oxidation Event (hereinafter the GOE), Archean seawater likely contained < 1mM sulfate (Holland, 1984; Canfield, 1998; Habicht et al., 2002; Farquhar and Wing, 2003; Kah et al., 2004; Jamieson et al., 2013; Crowe et al., 2014). The first occurrence of evaporitic sulfates at ca. 2.4-2.3 Ga suggests that marine sulfate concentration reached at least ~2.5 mM shortly after or during the GOE (Bekker et al., 2001; Schröder et al., 2008; Crockford et al., 2019). Further, recent reconstructions based on sedimentary sulfate, sulfide, and carbonate-associate sulfate spanning from ~2.0 Ga to 0.6 Ga suggest the marine sulfate from 2 to 10 mM (Halverson and Hurtgen, 2007; Blättler et al., 2018a, 2020; Turner and Bekker, 2016; Fig. 2). On the other hand, multiple studies suggest much lower

sulfate concentrations (0-5 mM) in the Paleo- and Mesoproterozoic and micromolar concentrations in the Archean based on absence of thick bedded massive sulfate evaporates, and minimal sulfur isotope fractionation between pyrite and carbonate associated sulfate (e.g. Fakhraee et al., 2019; Kah et al., 2004; Scott et al., 2014). Thus, the 2.41 Ga Vetreny Belt rocks occupy a peculiar place in the marine sulfate record, as they could have interacted with seawater containing a wide and growing range of sulfate concentrations. Conservatively, we rely on the timing of the first appearance of evaporitic sulfate at ~2.4-2.3 Ga (Schröder et al., 2008; Crockford et al., 2019) that likely occurred around the same time or after the formation of the Vetreny Belt. Consequently, we explore the hypothesis in which marine sulfate was low (~1 mM), reflecting generally high Ca/SO_4 ratios and, thus, limiting anhydrite precipitation in equilibrium with hydrothermal fluids. As we show later in the paper, the difference between choosing 1 to 10 mM sulfate as the initial marine concentration does not affect out interpretations significantly, due to consistently high Ca/SO_4 ratios. To support this, we explore a wide range of marine sulfate concentrations between 1 and 28 mM, and marine Ca between 10 and 40 mM.

2. METHODS

2.1 Sr isotope measurements

Strontium isotope ratios ($^{87}Sr/^{86}Sr$) were measured using the Nu Plasma HR multicollector inductively-coupled-plasma mass-spectrometer (MC-ICP-MS) hosted at the Geology Department of the University of Illinois, Urbana-Champaign. Silicate samples were dissolved with concentrated HF and HNO_3 in Teflon beakers, while carbonates were treated with concentrated HCl and HNO_3. After removing an aliquot of the solution for Rb and Sr concentration determination, the majority of the dissolved sample was loaded onto 200 μl Sr spec column for Sr purification. The sample was introduced to the mass spectrometer using an Aridus II desolvator. Standard NIST SRM 987 was run between every 3 samples and two other standards, Eimer and Amend and an in-house modern coral were run every 6 samples. All

samples and the two secondary standards were corrected for offsets in $^{87}Sr/^{86}Sr$ between the measured (0.71040 ± 0.00001; mean ± 1σ; n = 10) and nominal values of NIST SRM987 (0.71034 ± 0.00026). This correction results in accurate measurements for Eimer and Amend (0.70804) and modern coral (0.70918). The reproducibility of each sample is conservatively estimated as ± 0.00003.

The Rb and Sr concentrations were determined using a Thermo iCAP-Q ICP-MS. Quantification involved external calibration lines and admixed internal standards for drift. The uncertainty on the Rb/Sr ratios is conservatively estimated as ± 10 % of the mean.

2.2 Conventional O isotope measurements

The $\delta^{18}O$ values were determined in several amphibole separates and whole rock samples (n = 7) of altered gabbros from the Ruiga subvolcanic intrusion. The analyses were performed at the University of Oregon Stable Isotope Laboratory vacuum line using laser-assisted fluorination in the presence of BrF_5 to liberate O_2 from silicates. The product O_2 was subsequently purified through a series of cryogenic traps held at liquid N_2 temperature and a mercury diffusion pump. The gas was converted to CO_2 gas and subsequently analyzed with a MAT 253 mass spectrometer in dual-inlet mode. The average uncertainty on the $\delta^{18}O$ determination was ± 0.1 ‰. The accuracy of the analysis was monitored with the in-house standard UOG (University of Oregon Garnet standard; $\delta^{18}O$ = 6.52 ‰ VSMOW). A powdered sample of unaltered komatiitic basalt was analyzed using an airlock sample chamber. This allowed us to introduce and fluorinate one sample at the time avoiding high blanks due to the reactivity of powdered samples.

In addition, we measured C and O isotope composition of the two sedimentary carbonate samples from the Kozhozero suite. The analysis was conducted using the GasBenchII device connected to the DeltaXP mass spectrometer located at the University of Lausanne, Switzerland. The procedure is outlined in (Spötl and Vennemann, 2003). Briefly, powdered samples (100-300 µm) were reacted with phosphoric acid at 70 °C. The product CO_2 was separated from other

components using a gas chromatographic column and analyzed in the mass spectrometer for $\delta^{13}C$ and $\delta^{18}O$ values. The reproducibility of ± 0.06 and 0.08 ‰, respectively, was monitored by analyzing an in-house standard.

2.3 Fluid inclusions measurements by LA-ICP-MS

The chemical compositions of quartz-hosted fluid inclusions were measured using LA-ICP-MS at the Department of Earth Sciences of ETH Zurich (Switzerland). We used a Perkin Elmer NexION 2000 fast-scanning quadrupole ICP-MS connected to the ETH-prototype GeoLas laser ablation system equipped with a Coherent ComPex Pro 102F Excimer ArF (193 nm) laser source. For this study, we used assemblages of ~10-micron quartz-hosted fluid inclusions abundantly present in samples VB8A and GO22. These are the same samples that host epidote used for the isotope measurements (see Fig. 3E). The fluid inclusions consist of polyphase brines containing a liquid, a gas bubble and a halite crystal, frequently associated with vapor-like inclusions. Only the former yielded quantifiable signals upon ablation. We targeted tight clusters of brine inclusions showing very similar phase proportions that were therefore assigned as fluid inclusion assemblages (n = 13 in VB8A and n =10 in GO22).

The sample chips were set in a custom-made, small volume (ca. 1 cm^3) and fast-washout stainless steel ablation chamber, mounted on an optical microscope equipped with a CCD camera. Gas blanks and system contamination were minimized following the cleaning and setup recommended by Schlöglova et al. (2017). The ablation chamber was fluxed with He (ca. 1 L/min) as carrier gas to which was admixed make-up Ar (ca. 1 $L.min^{-1}$) downstream of the ablation chamber, prior to introduction in the plasma. The ICP-MS was optimized for maximum sensitivity on the whole mass range and low oxide rate formation ($^{248}ThO^+/^{232}Th^+ < 0.5\%$).

The NIST SRM610 glass (Jochum et al., 2011) was used as external standard for quantification of most elements, except S, Cl and Br that were calibrated against the Sca-17 scapolite standard (Seo et al., 2011). Both were analyzed with laser spot diameter of 40 μm, repetition rate of 10 Hz, energy density of ca. 7 J cm^{-1} and a ca. 1 min measurement consisting

of 30 s gas blank followed by 30 s ablation. For fluid inclusions, analyses were performed with a laser repetition rate of 10 Hz, energy density of ca. 15 to 20 J cm^{-2}, variable spot sizes set as to completely ablate the entire inclusion (see Heinrich et al. (2003) for details) and an ablation duration of ca. 1 min. The spot diameter was slowly incremented to the desired size using an opening aperture, to prevent quartz cracking (Gognon et al., 2003). Intensities for the following isotopes were acquired in peak jumping mode: ^{7}Li, ^{11}B, ^{23}Na, ^{25}Mg, ^{27}Al, ^{29}Si, ^{34}S, ^{35}Cl, ^{39}K, ^{42}Ca, ^{55}Mn, ^{57}Fe, ^{63}Cu, ^{66}Zn, ^{75}As, ^{79}Br, ^{85}Rb, ^{88}Sr, ^{133}Cs, ^{137}Ba, and ^{208}Pb with a dwell time of 10 ms except for Na, Al, Si, K, Sr and Ba (5 ms), corresponding to a total sweep time of 0.224 s.

Data processing was performed with the Matlab-based SILLS program (Guillong et al., 2008). The fluid inclusion signals were corrected for contributions from the host quartz using a SiO_2 content of 99.9 wt.% as internal standard. Spectra were only selected for element quantification if the ablation of the FI was controlled (i.e. not breached at the onset of ablation) and when the FI peak was clearly distinguishable from the surface contamination peak; Pettke et al., 2012). Over 100 inclusions were analyzed, of which 88 gave useable signals.

2.4 Reactive transport model in dual-porosity medium

We undertake reactive transport modeling of water-rock isotope exchange in a dual-porosity system (DePaolo, 2006) since we use epidote measurements from filled fractures and veins, where both advective and diffusive transport occurs. The model is used to calculate simultaneous shifts of Sr and triple O isotope ratios experienced by hydrothermal fluids. The principal equation includes diffusion, advection and reaction terms that add (dissolution) or consume (precipitation) chemical species:

$$\rho_f \frac{\partial \phi C_f}{\partial t} = \rho_f D \frac{\partial}{\partial x}\left(\frac{\partial \phi C_f}{\partial x}\right) - v\rho_f \frac{\partial \phi C_f}{\partial x} + \sum_i R_{\mathrm{d}i}\, C_{si} - \sum_j R_{\mathrm{p}j}\, K_j C_f \qquad (1),$$

where C is concentration of element in the fluid and solid (subscript f and s respectively), ρ and ϕ denote density and porosity, D is ionic diffusivity, v is fracture fluid velocity, K is distribution

coefficient for solid/fluid. The terms R describe rates of dissolution (subscript d) and rates of precipitation (subscript p) of species i and j.

The equation can be re-written for a fractured medium, where fluid transport occurs via advection along fractures and diffusion in the low-porosity matrix. Combining dissolution and precipitation into one term yields recrystallization rate (denoted R) expressed in $g \cdot g^{-1} \cdot yr^{-1}$, i.e. grams of alteration material forming per grams of original rock in a year. As explained in DePaolo, 2006, the steady-state assumption of the dual porosity model is a good starting point for demonstrating possible trajectories of combined isotope shifts. The application of such assumptions is justified by the relative longevity of hydrothermal systems and by our inability to make safe assumptions about how and why the isotopic ratio of incoming/discharging fluids changed with time, when only the final product (hydrothermally altered rocks) can be analyzed. In the steady-state formulation of the model, the fluid isotopic ratios change with distance (x in meters). The rate of change of isotopic ratio in fracture fluid (r_f) with the distance is described as (eq. 28 in DePaolo, 2006):

$$\frac{\mathrm{d}r_f(x)}{\mathrm{d}x} = \frac{8D\phi_m}{\phi_f v_f b d}\left[r_s - \alpha r_f(x)\right] \sum_{n_{odd}} \left(1 + n^2\pi^2 \frac{L^2}{b^2}\right)^{-1} \quad (2),$$

where D is ionic diffusivity of a species (e.g. self-diffusion of H_2O, Sr^{2+}), ϕ is porosity in the matrix, v_f velocity of the fracture fluid, ϕ_f porosity of the fracture (always equals 1), b is fracture spacing and d is fracture width. The variable L (reactive length) derives from the relationship $(D\rho_{fluid}\phi C_{fluid}/R\rho_{rock}(1-\phi)C_{rock})^{1/2}$, where ρ, ϕ, C denote density, rock porosity and concertation of an element of interest. The fractionation factor α is an equilibrium fractionation factor. For Sr, α is unity, i.e. no fractionation occurs, while O isotope fractionation can be described as $^{18/16}\alpha$ =1.002 for high-temperature bulk rock-H_2O fractionation of $^{18}O/^{16}O$ ratio. Fractionation of $^{17O/16}O$ follows the relation $^{17/16}\alpha = {}^{18/16}\alpha^{\theta}$ for, where θ is mass-dependent exponent appropriate for high-temperature fractionation of triple O isotope ratios, e.g. 0.529 (Matsuhisa et al., 1978; Pack and Herwartz, 2014).

The results of steady-state dual porosity model are dependent on the poorly constrained physical parameters such as reaction rates, fluid velocity, fracture spacing, and porosity (R, v_f, b and ϕ). These path-integrated variables are especially difficult to measure directly and perhaps should not be constrained by single values. The effects of changing the fracture spacing (b) and recrystallization rates (R) were discussed previously (DePaolo, 2006; Turchyn et al., 2013; Brown et al., 2013, 2020). It is sensible to accept the average fracture spacing on the order of several meters (1 m), while the recrystallization rates vary on the order of 0.0001 yr^{-1} as constrained from short-lived isotopes in active hydrothermal systems (Kadko and Moore, 1988; Kadko et al., 2007). Further, the ground water flow convects around intrusive bodies at rates anywhere between several meters a year, up to ~100 m/yr (Norton, 1978; Wood and Hewett, 1982; Hayba and Ingebritsen, 1997). Here we perform Monte-Carlo simulation of the isotopic shift using ranges of values listed in the Table 1. The isotopic shifts were calculated at ~200m (x in Eq. 2) 2000 times randomly picking variables from the uniform distributions within specified ranges. This value of x is used because it successfully reproduces the isotope shifts measured in modern-day oceanic hydrothermal fluids (see Discussion).

2.5 Mineral aqueous equilibrium calculations and Sr isotope balance

All calculations of seawater-basalt reaction with different concentrations of marine SO_4 and Ca were simulated following the same steps as described below allowing for convenient comparison. The starting seawater compositions for modern seawater-basalt reaction is taken from (Berner and Berner, 1996). For all other reactions, we modified the initial seawater by taking different SO_4 and Ca concentrations with the Mg concentration set to 45 mM. This number is close to the average estimate of Mg concentration in the seawater throughout the Phanerozoic (see Turchyn and DePaolo, 2019). The rest of solutes are left at the same concentrations compensating the charge by Cl^-. We acknowledge that seawater solutes in the Precambrian are not reconstructed as reliably as for the Phanerozoic owing to the absence of

412 suitable record, however using these values allows us to make a realistic comparison of the effect
413 of variable calcium/sulfate ratio.
414 We perform seawater-basalt reactions using the program CHIM-XPT (Reed et al., 2010)
415 to simulate a set of titration experiments in which small amount of basalt is incrementally added
416 to 1020 g (1L) of seawater and the solution is then allowed to achieve equilibrium concentrations
417 of aqueous species and minerals. A realistic order of events is simulated via following steps: 1)
418 reaction of small amount of basalt (5 g) at 150 °C and 400 bar and removal of solid phases at the
419 end; 2) reaction with another 5g of basalt at 350 °C and 500 bar and removal of solid phases at
420 the end; 3) titration of basalt until aqueous concentrations become dominated by equilibrium
421 with basalt. At this stage, albite and microcline molar quantities exceed other minerals. This
422 configuration is intended to reproduce hydrothermal system in which seawater first heats up to
423 ~150 °C with precipitation and removal of anhydrite and other oversaturated phases as they
424 occupy empty spaces, vesicles and pores, yet with minimal participation of basaltic material (Alt
425 et al., 1996; Fisher, 1998). Next, fluid moves through hot wall rock, precipitating minerals at
426 higher temperature and pressure (350 °C and 500 bar), leaving the minerals behind in a
427 permeable upper crust. Then fluid reacts with basalts at low water-rock ratios. The water-rock
428 ratio (W/R) in these calculations is used as a measure of titration progress; it is calculated from
429 dividing the amount of initial seawater (1020 g) by the mass of titrated basalt. Thus, step #1
430 described above represents seawater-basalt reactions at W/R between infinity (0 g basalt added)
431 and 204 (5 g basalt titrated).
432 The $^{87}Sr/^{86}Sr$ ratios of hydrothermal fluids are calculated from the simple mass balance
433 calculation. The contributions are derived from titrated basalt assuming that it contains 200 ppm
434 Sr (2.28 mmoles/g), and from the initial seawater Sr content and its isotope ratio. In calculating
435 the modern seawater-basalt reaction, we take 87 μmol/kg as the initial marine Sr concentration.
436 We use the marine Sr/Ca ratio of 9 μmol/mmol to retrieve the initial Sr concentrations in these
437 calculations, unless specified otherwise. This is justified since the reconstructed ratios have been

remarkably stable at ca. 8-9 μmol/mmol across the last 200 Ma (Coggon et al., 2010; Turchyn and DePaolo, 2019; Zhang et al., 2020). The simple mass-balance of Sr isotopes in the hydrothermal fluid in the initial stages of seawater-basalt reaction is expressed as:

$$^{87}Sr/^{86}Sr_{fluid}\,([Sr]_{anhydite} + [Sr]_{fluid}) = ([Sr]_{SW}\,^{87}Sr/^{86}Sr_{SW} + [Sr]_{basalt}\,^{87}Sr/^{86}Sr_{basalt}) \quad (3),$$

where dissolved ions and anhydrite (if present) are the only Ca- and Sr-bearing species on the left-hand side. As more basalt added, more Sr-bearing phases (e.g. epidote) appear on the left-hand side of the equation (Eq. 3), while anhydrite is removed at steps #1 and #2 (see paragraph above). We assume no isotope fractionation across phases on the left-hand side, thus we assume same $^{87}Sr/^{86}Sr$ of equilibrium fluids and minerals. The Sr concentration contained in equilibrium anhydrite and in the fluids are then calculated from the distribution coefficient K_D:

$$\frac{[Sr]_{anhydrite}}{[Sr^{2+}]_{aqm}} = K_D * \frac{[Ca]_{anhydrite}}{[Ca^{2+}]_{aqm}} \quad (4).$$

The $[Ca]_{anhydrite}$ and total dissolved Ca contained in fluid $[Ca^{2+}]_{aqm}$ are given by the output of the mineral-aqueous equilibrium modeling in CHIM-XPT. To keep track of Sr concentration, we specified a distribution coefficient between anhydrite and fluid (K_D) expressed as $[Sr/Ca]_{anhydrite}/[Sr/Ca]_{fluid} = 0.6$ (Mills et al., 1998; Teagle et al., 1998). Additionally, we explore the effect of changing the K_D to 0.4 and 0.9. Such values encompass the majority of distribution coefficients observed during rapid precipitation of anhydrite (Syverson et al., 2018).

Following the procedure outlined above, we performed two sets of calculations. The *first set* features a detailed calculation of seawater-basalt reaction using i) modern seawater composition as initial fluids and ii) the envisioned 2.41 Ga seawater compositions, where Ca, Sr and SO_4 concentrations were taken as 20 mmol/kg, 160 μmol/kg and 1 mmol/kg, respectively. This set is carried out over a wide range of W/R and with enabled computation of solid solutions. The compositions of reactants are summarized in Table 2. The Sr concentration is taken from the results of the fluid inclusion measurements, while SO_4 represents a hypothesized value based on

463 the projected marine sulfate concentrations. In addition, we tested for the difference in using
464 high-Mg (MgO = 12.4 wt. %) and normal mid-ocean ridge basalts (MgO = 7.8 wt. %; Table 2)
465 as reactants in our calculations, since the Vetreny Belt rocks include abundant komatiitic basalts.
466 Since the exact concentration of sulfate in initial seawater is not reliably constructed for
467 2.43 – 2.41 Ga seawater we also carry out *second set* of calculations using a wide range of SO_4
468 concentrations between 1 mmol/kg and 28 mmol/kg. These numbers represent the reported
469 estimates throughout the Proterozoic and Phanerozoic sulfate concentrations (Holland, 1984;
470 Lowenstein et al., 2003; Fakhraee et al., 2019; Blättler et al., 2020). Calcium was varied between
471 10 and 40 mmol/kg. This set of calculations was performed across multiple seawater Ca/SO_4
472 ratios, above and below 1, for a range of W/R defined by the reaction with pristine seawater
473 (W/R infinity) and by first appearance of epidote (W/R of ~ 50). This offers a sensitivity test for
474 the $^{87}Sr/^{86}Sr$ measurements of epidotes as a tracer of the marine Sr at variable marine Ca/SO_4
475 values. Since many calculations were performed, we disabled calculation of solid solutions.

476 **3. RESULTS**

477 **3.1 Elemental concentrations measured in fluid inclusions**

478 The data is reported here (Tables 3 and 4) in two ways: (1) as assemblage ratios to Na
479 (Table 3), which should be preferred for interpretation given that salinity was not directly
480 determined; and (2) as concentrations (ppm) calculated using an average salinity of 40 wt.%
481 NaCl equivalent (average salinity obtained for the inclusions by microthermometry) and a
482 correction accounting for the presence of other cations as major chloride compounds (i.e. K, Ca
483 as well as Fe and Mn for sample VB8A), determined based on the raw intensity ratios (Table 4).
484 The Na-normalized ratios could be used to recalculate concentrations using any salinity. Further,
485 Supplementary Table 1 contains both the results of individual fluid inclusions analyses and the
486 calculated averages for the corresponding assemblages with corresponding uncertainty (standard
487 deviation of the n individual inclusion signals used to calculate the average composition of the

assemblage). The limits of detection (LOD) listed in the Supplementary Table 1 were calculated using the method of Pettke et al., (2012) and are reported for individual inclusion analyses.

In this study we focus on elemental ratios that reflect modification of original seawater signature due to its reaction with basalt and due to phase separation, particularly Cl/Br, Na/K, Ca/Na and Sr/Na ratios (Fig. 5). Notably, the fluid inclusions of the two samples have distinct Cl/Br ratios; the values range mostly between 24-40 and 200-1000 for VB8A and GO22 respectively. The Sr concentrations in the fluid inclusions (expressed as Sr/Na) range from 0.0013 to 0.0087 in sample GO22, while the VB8A displays elevated ratios between 0.0516 and 0.1526.

3.2 $^{87}Sr/^{86}Sr$ values

The $^{87}Sr/^{86}Sr$ and Rb/Sr ratios of the Vetreny Belt epidotes, altered pillow basalts, unaltered komatiitic basalts and underlying carbonates along with modern oceanic epidotes included in this study are summarized in Figure 6 and reported in Table 5. The $^{87}Sr/^{86}Sr_{initial}$ values are calculated based on the age of lithologies of the Vetreny Belt. The mean and uncertainty include propagated errors from the maximum possible uncertainty in age (2.42±0.01 Ga), analytical error of isotope measurements (±0.00003) and the error in Rb/Sr ratio (±10 %), yielding a total range of uncertainties between 0.00003 and 0.00071 (± 1σ). The $^{87}Sr/^{86}Sr_{initial}$ values of epidote are the most precise due to their low Rb/Sr (see Table 5). The Rb concentrations in epidotes are below the detection limit of ~1ppm. The unaltered rock samples have $^{87}Sr/^{86}Sr_{initial}$ values in the range 0.7008-0.7016; these values are typical for the contemporaneous composition of ultramafic melts, slightly contaminated by crustal material (Puchtel et al., 1997, 2016). Altered pillow rinds and epidotes have $^{87}Sr/^{86}Sr_{initial}$ ratios between 0.7029 and 0.7042, significantly higher than that of the unaltered rock. The two samples from the underlying carbonate unit of Kozhozero suite returned Rb/Sr ratios of 0.006 and 0.016 and the $^{87}Sr/^{86}Sr_{initial}$ of 0.7045-0.7046 (Fig. 6), close to the previous measurements of marine carbonates (Fig. 1; Kuznetsov et al., 2010). We note that upon preparation of the carbonate samples, some

514 solid residue remained undissolved. Consequently, the carbonates of the Vetreny Belt require
515 more effort to assess their origin and the integrity of marine isotope signal.

516 **3.3 $\delta^{18}O$ values**

517 The $\delta^{18}O$ values of amphibole separates and whole rock samples from the Ruiga intrusion
518 range between -0.7 and +3.0 ‰ (Table 6). They are plotted on the schematic geologic map in
519 Figure 4. The unaltered komatiitic basalt (sample 12105; see sample 91105 in Puchtel et al.
520 1996) returned $\delta^{18}O$ value of +5.6 ‰. The two samples of sedimentary carbonates from the
521 Kozhozero suite returned $\delta^{13}C$ values of -0.95 and -1.38 ‰ and $\delta^{18}O$ of -27.8 and -28.3 ‰
522 VPDB. The previously measured $\delta^{18}O$ – $\Delta'^{17}O$ values of modern and ancient samples are
523 combined with the $^{87}Sr/^{86}Sr$ values in Figure 7. The $\delta^{18}O$ are plotted as the linearized notation
524 $\delta'^{18}O = 10^3\ln(1+\delta^{18}O/1000)$. The triple O isotope values of ancient and modern oceanic epidote
525 are compiled from (Zakharov and Bindeman, 2019; Zakharov et al., 2019b) and recalibrated to
526 the VSMOW-SLAP defined scale with the San Carlos Olivine values of $\delta^{17}O$ = 2.668, $\delta^{18}O$ =
527 5.153 and $\Delta'^{17}O$ = -0.049 ‰. The value is slightly modified from (Pack et al., 2016) and
528 represents unification of the standardization efforts (Pack et al. 2016; Wostbrock et al., 2020) by
529 subtracting 12 ppm from the $\delta^{17}O$ of original value. The stretching and shift are determined from
530 the analyses of KRS-SKFS standards measured at the University of Oregon (Miller et al. 2020).
531 The recalibration scheme is presented in Herwartz (2021) along with our previous measurements
532 of hydrothermally altered rocks. The recalibrated values are gathered in Supplementary Table 2.

533 **3.4 The output of dual-porosity model and Montel-Carlo simulation**

534 The results of the dual-porosity model are presented in Figure 7. For verification of our
535 approach, we show the result of conventional $\delta^{18}O$ – $^{87}Sr/^{86}Sr$ profiles with the previously
536 published data on hydrothermal fluids (Bach and Humphris, 1999) and epidotes measured here
537 (Fig. 7A). In addition, we show the profiles in the $\Delta'^{17}O$ – $^{87}Sr/^{86}Sr$ space with modern and
538 ancient oceanic epidote presented here. The outputs are shown as the 2D-density distributions

(Fig. 7) of isotope shifts produced by the ranging values of reaction rates, porosity, fluid flow and fracture spacing as constrained by previous studies (see Methods).

3.5 Equilibrium mineral assemblages and aqueous speciation

The equilibrium Ca-bearing minerals and several other selected minerals are shown in Figure 8. The total molality of dissolved species and moles of all mineral species during the reactions are shown in Figure 9. As expected, these calculations show that the abundance of anhydrite is the most noticeable difference between high- and low-sulfate seawater-basalt reactions. The fraction of marine Sr incorporated into the equilibrium minerals is expressed as $[^{87}Sr/^{86}Sr_{mineral} - {}^{87}Sr/^{86}Sr_{basalt}]/[^{87}Sr/^{86}Sr_{SW} - {}^{87}Sr/^{86}Sr_{basalt}]$, where subscripts *SW* and *basalt* denote seawater and unaltered rock with their initial $^{87}Sr/^{86}Sr$. In the calculation with 1 mM sulfate and 20 mM Ca (envisioned for 2.41 Ga seawater), the maximum amount of marine Sr incorporated in epidote is 80 %. We found no significant difference in the computed $^{87}Sr/^{86}Sr$ epidote values produced by a reaction with high-Mg basalt with 12.4 wt. % MgO (see Supplementary Text 1). Meanwhile, in the modern seawater-basalt reaction, epidote contains up to 27 % marine Sr. Our results show that the possible variations in the distribution coefficient K_D (Syverson et al., 2018) play a relatively minor role compared to the effect of abundant anhydrite precipitation (Fig. 8). The range of W/R where epidote is sensitive to the difference in marine sulfate concentrations is between 10 and 50. Further, we notice that in the calculation with 1 mM sulfate, the first appearance of epidote occurs at slightly higher W/R compared to the calculation with modern seawater concentration of solutes. This is due to the relatively higher concentration of aqueous Ca in sulfate-poor reaction. This translates into a higher $^{87}Sr/^{86}Sr$ ratio of the early-formed epidote in the low sulfate calculation. In addition, in the calculation with 1 mM sulfate, epidote is comparatively rich in the aluminous endmember, clinozoisite. Both calculations show a similar pattern of becoming more clinozoisite-rich with decreasing W/R.

4. DISCUSSION

We first need to discuss the fluid inclusion data as they allow us to directly determine the Sr concentrations in ancient hydrothermal fluids independently of the isotope data. Using those estimates, we can test for the marine Sr transfer within the 2.41 Ga hydrothermal system.

4.1 Constraints from fluid inclusion measurements

The composition of fluids trapped in these samples resulted from the reaction of seawater with rocks at high temperature and phase separation of the fluids. Phase separation could lead to elevated Sr concentrations in hydrothermal fluids proportional to the increase in salinity (e.g. Butterfield et al., 1990). The types of fluid inclusions in these samples include both highly saline halite-saturated inclusions that homogenize to liquid, and vapor-dominated inclusions that homogenize to vapor (Fig. 5A). Therefore, to assess the effect of phase separation, we use the Cl/Br ratio as it fractionates during precipitation or dissolution of halite, since Br is incompatible. Compared to modern seawater, these brines are about 8-11 times more saline (Zakharov and Bindeman, 2019). The Cl/Br ratios in sample GO22 overlap with those of seawater, be it modern (600) or reconstructed Archean (400; De Ronde et al., 1997), which suggests that this sample hosts the least modified fluids. In contrast, the fluids hosted in VB8A were perhaps affected by more advanced halite-brine fractionation and phase separation that decreased the Cl/Br and Na/Br ratios. Further, the sample VB8A exhibits elevated concentrations of elements that have affinities with brines, like K, Ca, Fe, Mn, Zn, etc. (see Table 3). The Sr/Na ratios measured by LA-ICP-MS in sample GO22 range from 0.0013 to 0.0087 close to that of seawater, mimicking the pattern exhibited by Ca/Na ratios (Fig. 5B). The possible variations in Sr/Na caused by halite-fluid fractionation and/or phase separation would likely be within the large uncertainties of these ratios (± 37 % relative, on average), so that this range should be reasonably representative of seawater that underwent minimal exchange with basaltic rocks. Assuming that the seawater salinity did not change significantly through time, the corresponding Sr concentration estimated from the GO22 fluid is between 14 and 94 ppm, or 160-1073 μmol/kg, with an average of 457 μmol/kg. This range can be interpreted as pre-phase-separation

590 Sr concentrations varying between seawater and the hydrothermal fluid, respectively. These
591 estimated figures are realistic based on the modern and reconstructed Phanerozoic marine Sr
592 concentrations. For example, modern seawater contains 87 μmol/kg Sr, while the seawater Sr
593 concentration of Cretaceous and Ordovician seawater is estimated to be ~570 μmol/kg (Coogan,
594 2009; Turchyn and DePaolo, 2019). Thus, for the rest of the discussion we accept that the least
595 modified fluid, i.e. seawater, had about 160 μmol/kg Sr, i.e. the value least affected by phase
596 separation and contributions from basaltic source.

597 **4.2 Marine Sr recorded in epidote of the Vetreny Belt**

598 The high input of marine Sr in the hydrothermal system of the Vetreny Belt is evident
599 from the epidote $^{87}Sr/^{86}Sr_{initial}$ values ranging between 0.70288 and 0.70422, significantly higher
600 than 0.701, an average value of the unaltered fresh basalt (Fig. 6). Further, the bulk altered
601 basalts of the Vetreny Belt, including altered hyaloclastites and altered pillow rinds, also display
602 high $^{87}Sr/^{86}Sr_{initial}$ ratios, between 0.7029 and 0.7042, consistent with alteration at high W/R and
603 high input of marine Sr. These values are exceptionally high and hint at seawater $^{87}Sr/^{86}Sr$ above
604 0.704, close to the values of the underlying carbonates of the Kozhozero suite. However, caution
605 is used when interpreting the carbonate samples as the record of pristine seawater value, as they
606 were likely modified in post-depositional environment. In combination with previous
607 investigations of the early Paleoproterozoic formations (Bekker et al., 2001, 2003; Kuznetsov et
608 al., 2010), we suggest that the ca. 2.41 Ga seawater might have been as high as 0.7045 in
609 $^{87}Sr/^{86}Sr$. That would translate into ~90 % of marine Sr incorporated into the Vetreny Belt
610 epidote. The extent of connectivity to the global ocean could potentially affect our interpretations
611 as the local seawater could be influenced by the cratonic runoff. Yet, the relatively long Sr
612 residence time (~2.5 Ma; Hodell et al., 1990) and the circulation time (~1500 years; Broecker
613 and Peng, 1982) of the modern ocean together result in its well-mixed $^{87}Sr/^{86}Sr$ ratio, even in
614 partially restricted basins, for example, in Red Sea (see Craig, 1966). Thus, it is logical (see

615 Discussion in Satkoski et al., 2016) to suggest that the Vetreny Belt was also representative of
616 the global marine Sr.

617 Epidote and hydrothermally altered basalts of modern oceanic crust and ophiolites
618 indicate that on average 20-50 % of marine Sr reaches the high-temperature alteration zones of
619 oceanic crust (Fig. 6; Kawahata et al., 1987; Bickle and Teagle, 1992; Alt et al., 1996; Harris et
620 al., 2015). Higher values are measured in epidote from Cretaceous and Ordovician ophiolite
621 sequences (McCulloch et al., 1981; Bickle and Teagle, 1992; Alexander et al., 1993; Turchyn et
622 al., 2013; Antonelli et al., 2017), coinciding with periods when oceans were low in sulfate (≤10
623 mM; Berner, 2004). For comparison, we show the detailed $^{87}Sr/^{86}Sr$ systematics of the Troodos
624 ophiolite rocks, provided in the study by Bickle and Teagle (1992), where the fraction of marine
625 Sr reaches 60-70 % in epidosites and altered basalts. As suggested previously, these observations
626 conform to the link between seawater Ca/SO_4 ratio and isotope budget of hydrothermal fluids
627 (Fig. 3 in Antonelli et al., 2017). Thus, it appears logical that when Earth's surface had limited
628 capability to produce abundant sulfate, namely at 2.41 Ga, and the Ca/SO_4 were generally high,
629 this effect should be even more extreme, and submarine hydrothermal fluids were even more
630 enriched in radiogenic seawater-derived Sr as depicted with the Sr isotope values of the Vetreny
631 Belt rocks. In the following section, we test the extent of modification of original seawater
632 signature by seawater-basalt reaction using the combined triple O and Sr isotope approach.

633 **4.3 Conventional $\delta^{18}O$ values and combined $\delta^{18}O$ – $\Delta'^{17}O$ – $^{87}Sr/^{86}Sr$ approach**

634 First, we need to point out that the conventional $\delta^{18}O$ measurements presented here
635 document a typical mantle value of $\delta^{18}O$ = +5.6 ‰ (e.g. Eiler et al., 2000) in the well-preserved
636 unaltered rocks of the Vetreny Belt. The high temperature altered plutonic section measured at
637 the Ruiga intrusion has $\delta^{18}O$ between -0.7 and +3.0 ‰ (Fig. 4), similar to the distribution of
638 values within modern altered oceanic crust (Alt and Teagle, 2000; Alt and Bach, 2006). The
639 $\Delta'^{17}O$ of the unaltered basalt was not measured directly, yet the variability in terrestrial mafic
640 rocks is limited to -0.05 ± 0.01 ‰ (Pack and Herwartz, 2014; Sharp et al., 2018; Cano et al.,

641 2020). Based on our previous fluid inclusion and O isotope thermometry measurements
642 (Zakharov and Bindeman, 2019), the estimated triple O isotope composition of the least-
643 modified seawater is $\delta^{18}O$ = -1.7 ‰ and $\Delta'^{17}O$ of around 0 ‰, close to the values of ice-free
644 oceans (Zachos et al., 2001). This slightly negative $\delta^{18}O$ value explains the slightly negative
645 values measured in the altered gabbros. The conventionally determined $\delta^{18}O$ of the carbonates
646 disagree with precipitation from such seawater. In fact, the measured values of ca. -28 ‰ VPDB
647 are lower than the values typical for carbonates of similar age (Shields and Veizer, 2002). Such
648 low $\delta^{18}O$ values are unlikely to reflect original deposition in marine environment and may have
649 been caused by precipitation from either really low $\delta^{18}O$ fluids or much higher temperature
650 above 300 °C (O'Neil et al., 1969). One potential explanation would entail diagenesis in
651 presence of glacial meltwaters, as the early 2.44-2.41 Ga Huronian glacial episodes are nearly
652 contemporaneous (Bekker et al., 2020) and are in fact recorded through extremely low ^{18}O-
653 depleted rocks on the Baltic Shield (Zakharov et al., 2019a). Recrystallization and alteration of
654 original isotope signal at high temperature in the presence of meteoric waters are also among the
655 reasons potentially responsible for such a low value (see Ryb and Eiler, 2018). Because
656 carbonates are prone to diagenesis and recrystallization, we rely on the triple O isotope
657 reconstructions of seawater values documented in Zakharov and Bindeman (2019).

658 Next, by comparing the $\Delta'^{17}O$-shifts recorded by modern and ancient epidotes (Fig. 7),
659 we note that the 2.41 Ga fluids of the Vetreny Belt likely experienced a similar amount of
660 interaction with basalt as those in modern submarine systems. Both ancient and modern epidotes
661 range in values between that of seawater and fluids in equilibrium with basalt, i.e. between -0.06
662 and 0.00 ‰ (Fig. 7A). This suggests that the Sr concentration of the fluid controlled the
663 distinctly high $^{87}Sr/^{86}Sr$ of the epidotes relative to contemporaneous seawater, not the difference
664 in the amount of seawater-basalt exchange (Fig. 7A). The shape of multi-isotope shifts in the
665 $\delta^{18}O$ – $\Delta'^{17}O$ – $^{87}Sr/^{86}Sr$ coordinates defined by epidote requires high Sr concentration in the
666 fluid, similar to that in the rock ($C_{fluid}/C_{rock} \approx 1$ in Eq. 2), even if we consider the effect of

667 different fracture spacing and the range of fractionation factors for epidote-H_2O (Figs. 7B and
668 7C). An average unaltered basaltic rock from the Vetreny Belt has 200 ppm Sr (Puchtel et al.,
669 1996), therefore requiring the fluids to have around 200 ppm Sr too. This contrasts with the 7-8
670 ppm Sr (80-90 μmol/kg) in modern seawater and its high sulfate concentration, which together
671 results in an abrupt shift of $^{87}Sr/^{86}Sr$ measured in upwelling fluids and epidotes, while their O
672 isotope values are moderately shifted (Fig. 7B; Alexander et al. 1993; Alt et al. 1996; Coogan
673 2009; Bach and Humphris 1999). This is also consistent with the estimated value of 160 μmol/kg
674 (~14 ppm) that represents the fluid Sr concentration prior to phase separation.
675 We use the Monte Carlo simulations of the dual-porosity model (DePaolo, 2006) to
676 portray possible ranges of the two-element isotope evolution of hydrothermal fluids. Overall, we
677 find that the output of the model agrees well with the modern data, where both the isotope
678 composition of seawater and Sr concentrations are known. We find that only limited variability
679 in the shape of the two-element trajectories can be produced by variable reaction rates, fluid
680 flow, fracture spacing, and porosity compared to the effects of drastically different concentration
681 of Sr in initial seawater. Further, this modeling approach allows us to compare fluid and epidote
682 values, as both record fluid flow in the fractured medium.
683 In summary, we consider the high $^{87}Sr/^{86}Sr$ of Vetreny Belt epidote to be a result of
684 several factors: i) initially high $^{87}Sr/^{86}Sr$ values (ca. 0.7045) of seawater; ii) moderate
685 concentration of marine Sr (~160 μmol/kg) that was subsequently increased by phase separation;
686 and iii) absence of anhydrite at the early stages of hydrothermal circulation. Further, the
687 consistency of the new $\delta^{18}O$ -- $\Delta'^{17}O$ -- $^{87}Sr/^{86}Sr$ data measured in epidotes from the 2.41 Ga and
688 modern oceanic environments contributes to the long-standing debate on the isotope evolutions
689 of seawater through time. The debate is based on the observation of consistently lower O isotope
690 values of the early Phanerozoic and Precambrian carbonates and cherts compared to modern-day
691 and Cenozoic counterparts (Knauth, 2005; Prokoph et al., 2008). Recent data on marine oxides
692 also document this trend (Galili et al., 2019). The observation has been interpreted in several

non-exclusive ways such as alteration by low $\delta^{18}O$ meteoric waters, smaller O isotope fractionation in hot Precambrian oceans (up to 70 °C) and/or significantly lower $\delta^{18}O$ values of seawater, down to -15 ‰ in the Archean (Shields and Veizer, 2002; Knauth, 2005; Jaffrés et al., 2007; Prokoph et al., 2008; Zakharov et al., 2021). If one accepts the hypothesis of changing marine $\delta^{18}O$ value, then early Paleoproterozoic cherts and carbonates indicate that seawater was ~8-9 ‰ lower than we reconstruct based on the triple O isotope approach. Our data suggests that the seawater O isotope values at 2.41 Ga were not significantly different from the Cenozoic (i.e. ice-free) hydrosphere. While it is not possible to reconstruct the ambient seawater temperature from altered basalts, we suggest that the alternative hypotheses or a combination of factors (higher seawater temperature and diagenesis) are more probable causes to the observed sedimentary trend.

4.4 The effect of different Ca/SO_4 ratios on incorporation of marine Sr

Amongst redox-sensitive marine species, sulfur is abundantly present in modern seawater due to the high solubility of its oxidized form, sulfate, causing oversaturation of seawater with anhydrite at temperatures above 150 °C (Fig. 1). As explained in Antonelli et al. (2017), the marine Ca/SO_4 ratio determines the amount of anhydrite distributed between the low- and high-temperature parts of oceanic hydrothermal systems (Fig. 1). During periods of low sulfate concentrations, when the Ca/SO_4 ratios are high, above 1, the amount of anhydrite precipitation is mostly limited to the low-temperature, early stages of alteration of oceanic crust (see Fig. 8). At this stage, when sulfate is removed as anhydrite, the excess of marine Ca and Sr is incorporated further downstream into the silicate minerals of altered crust. When the Ca/SO_4 ratios are < 1, like in modern seawater, the excess sulfate precipitates as high-temperature anhydrite with Ca and Sr derived from mixed marine and basaltic sources, and a proportionally smaller amount of marine Sr is incorporated into the silicate minerals like epidote.

In our equilibrium calculations we show how the modern and envisioned 2.41 Ga seawater-basalt reactions affect the distribution of marine Sr across mineral and aqueous species.

719 In the modern-day seawater-basalt reaction, anhydrite precipitates early in the titration, at 150
720 °C, W/R above 100, and thus, reflects $^{87}Sr/^{86}Sr$ values close to original seawater (Fig. 8), similar
721 to anhydrites from modern hydrothermal systems (e.g. Mills et al., 1998). The contribution of Sr
722 derived from further reaction with basalt shifts the $^{87}Sr/^{86}Sr$ of fluids from the high seawater
723 value towards the low basaltic value. In our high-sulfate calculation at 350 °C, which mimics the
724 modern high-temperature altered oceanic crust, the mineral assemblages include epidote with 10-
725 30 % marine Sr (Fig. 8) in agreement with the modern high-temperature vent fluid and epidote
726 values ($^{87}Sr/^{86}Sr$ = 0.702-0.704; Bach and Humphris 1999; Gillis et al. 2005; Harris et al. 2015).
727 The computed 2.41 Ga seawater-basalt reaction shows that the Ca-silicates and fluids at
728 W/R between 10 and 50 contain up to 80 % of original marine Sr. In addition, epidote in this
729 calculation forms earlier at slightly higher W/R when compared to the high-sulfate reaction. This
730 indicates that a high Ca/SO_4 ratio of seawater will promote an early capture of marine Sr by
731 epidotes. The mineral assemblages informative of the early capture of marine Sr by epidote can
732 be recognized by the presence of quartz but absence of feldspars, i.e. quartz-epidote veins. This
733 provides an additional support to our sampling strategy at the Vetreny Belt and enables
734 recognition of useful samples for the studies of paleoseawater $\delta^{18}O$, Ca/SO_4 and $^{87}Sr/^{86}Sr$ ratios.
735 Further, the Ca/SO_4 ratio might have dynamically evolved in the early Paleoproterozoic,
736 in concert with the rapid changes in oxidative capacity of weathering shortly after the GOE
737 (Scott et al., 2008). We explore the sensitivity of the $^{87}Sr/^{86}Sr$ epidote ratios using the simplified
738 seawater-basalt calculation over the range of Ca/SO_4 ratios (*second set*, see Methods). Shown as
739 color-coded points (Fig. 10), we calculated the $^{87}Sr/^{86}Sr$ of the early-forming epidote at W/R ~
740 50. Spanning the envisioned conditions of the early Paleoproterozoic and the Phanerozoic, the
741 resulted $^{87}Sr/^{86}Sr$ range between 31 % and 89 % of the original seawater value (Fig. 10).
742 Qualitatively the pattern is consistent with the concentrations of seawater solutes across the
743 Phanerozoic. However, only the Ordovician and modern epidotes match the quantitative output
744 of our calculation within several %. Cretaceous, Jurassic and Silurian epidotes yield consistently

lower values than those predicted by the calculation. Importantly, our results show that the $^{87}Sr/^{86}Sr$ value of epidote is sensitive to marine Ca/SO_4, especially early in the progress of seawater-basalt interaction. The sensitivity to marine Ca/SO_4 drops at low W/R because the values become overwhelmed by the basaltic signal. Thus, the lower marine Sr fraction incorporated in Cretaceous, Jurassic and Silurian can be explained by sampling epidotes that formed at lower W/R. Mechanistically, such epidote may have formed in an environment where advective transport was limited. Equilibrium fluids would have $^{87}Sr/^{86}Sr$ ratios significantly shifted towards basaltic values as shown in the models with small fracture spacing (Fig. 7).

4.5 Implications for the long-term marine Sr cycle

After the GOE, when marine sulfate reached several mM (Schröder et al., 2008; Blättler et al., 2018, 2020), hydrothermal circulation of seawater involved precipitation of anhydrite in considerable amount, compared to the envisioned low-sulfate Archean oceans. In the modern global geochemical balance, the dependency between anhydrite formation and removal of Ca and S from seawater is counter-balanced by the retrograde solubility of anhydrite at low temperature, below about 150 °C (see Fig. 1). However, the actual anhydrite fate likely depends on the history of individual fragments of oceanic crust, their cooling and sedimentation rates, as some anhydrite is still found in old oceanic crust (Alt et al., 2003). In addition, there is also evidence for subduction of seawater-derived sulfate into melt-generating reservoirs recorded by sulfur isotope studies of arc magmas (e.g. De Hoog et al. 2001) and eclogites (e.g. Evans et al. 2014). Further, considering the global S isotope budget models, only up to ca. 35 % of oceanic burial flux is in form of sulfide (Halevy et al., 2012; Tostevin et al., 2014). Thus, some amount of anhydrite stays in the crust, even though the co-existing seawater would become undersaturated with respect to the mineral at temperatures < 150 °C. This is likely due to the decreasing permeability of oceanic crust over time (Fisher, 1998). Yet the proportion of dissolved anhydrite vs anhydrite that ‘sticks around’ is difficult to estimate. Despite this uncertainty, it is likely that at least some of Ca, Sr and S that make up hydrothermal anhydrite

771 return into the ocean. Dissolution of anhydrite is, however, unlikely to play a significant role in
772 the isotope budget of oceanic Sr. It likely acts similarly to the diagenetic flux of Sr (Kump,
773 1989). That is to say that the Sr is released quickly from dissolution of anhydrite with the isotope
774 ratio similar to contemporaneous seawater. Such flux does not induce changes in the $^{87}Sr/^{86}Sr$ of
775 seawater, however, if this flux is large, it would buffer changes in the seawater $^{87}Sr/^{86}Sr$ caused
776 by changes in continental weathering.
777 In the early Precambrian oceanic crust, when oceanic Ca/SO_4 ratios were very high,
778 marine Sr should be permanently stored due to low solubility of high-temperature Ca-silicates
779 that contain Sr as a common trace element. In envisioned Archean oceans with sub-mM sulfate
780 concentrations, only negligible amounts of anhydrite formed, promoting a massive flux of
781 marine Sr into the high temperature altered oceanic crust. As documented in the present study
782 during the early Paleoproterozoic, when marine sulfate reached several mM (Schröder et al.,
783 2008), the mechanism of Sr burial likely involved comparatively minor anhydrite. Consequently,
784 a high fraction of marine Sr was constantly buried in the silicates of altered oceanic crust that
785 would eventually be subducted at convergent margins. In other words, the altered oceanic crust
786 was acting as a permanent sink for marine Sr.
787 In modern oceanic budgets, most of the Sr and Ca are from continental erosion delivered
788 by riverine fluxes (e.g. Palmer and Edmond 1989). As for the early Paleoproterozoic, the
789 proposed emergence of extensive landmasses (e.g. Flament et al. 2008; Bindeman et al. 2018),
790 continental break-up, global glaciations (e.g. Young 2013) and elevated atmospheric pCO_2 levels
791 (e.g. Sheldon, 2006) at the Archean-Proterozoic boundary would have enabled the riverine
792 delivery of Ca and Sr from eroded continental crust, while the limited oxidative capacity of
793 atmosphere sustained a relatively diminished flux of oxidized sulfur into the ocean. We suggest
794 that since the altered oceanic crust was acting as a permanent sink for radiogenic marine Sr, the
795 contribution of Sr derived from continental weathering was subdued in the overall oceanic
796 budget. This suggests that the Precambrian seawater $^{87}Sr/^{86}Sr$ curve would not only be a function

of radioactive decay of ^{87}Rb, continental growth, assemblies and break-ups (e.g. Halverson et al., 2007), but also would be dependent on anhydrite saturation within altered oceanic crust. In essence, we document the evidence that the evolution in marine Ca/SO_4 ratio changed the mechanisms of Sr burial. Yet, the magnitude of this effect exerted on the global Sr isotope budget is uncertain and proportional to the fraction of anhydrite that undergoes dissolution. The potentially ephemeral nature of anhydrite in modern-day oceanic crust versus permanent storage of Sr in silicates of ancient oceanic crust illustrate the importance of minimal sulfate precipitation on the oceanic Sr and Ca cycles.

5. CONCLUSIONS

We studied 2.41 Ga oceanic hydrothermally altered rocks from the Vetreny Belt, Russia that recorded interaction with seawater shortly after or during the GOE. Our study is overall consistent with a high marine Ca/SO_4 ratio, above 1, comparable to the upper range of the Phanerozoic values. In summary, we found:

1. The fluid inclusion elemental ratios (Cl/Br, Na/Br, Sr/Na) determined by LA-ICP-MS document near-seawater values in one sample and allow us to assess the effect of phase separation of the fluids that formed the quartz-epidote veins of the Vetreny Belt. Accounting for the salinity-increase, the reconstructed least-modified seawater had about 160 μmol/kg (or 14 ppm) Sr.
2. The $^{87}Sr/^{86}Sr_{initial}$ values of epidote and altered basalts fall between 0.7029-0.7042 indicating a high influx of marine Sr into the high-temperature alteration zones of the Vetreny Belt. Assuming that the 2.41 Ga seawater had $^{87}Sr/^{86}Sr = 0.7045$, these samples represent ~90 % marine Sr.
3. Triple O- and Sr-isotope approach combined with the reactive circulation modeling suggest that modern and ancient epidotes record similar amount of water-rock interaction and point out a difference in the behavior of Sr. Consequently, the Vetreny Belt epidote is best

explained by the high influx of marine Sr that was a) likely uninhibited by massive anhydrite precipitation and b) enhanced by phase separation.

4. Mechanistically controlled by Ca/SO_4 ratio in seawater, epidotes remain sensitive to marine Sr over a range of W/R between 10 and 50 as shown in our equilibrium seawater-basalt reaction calculations. Further, the calculations show that the equilibrium assemblage of quartz and epidote in absence of feldspars is particularly useful to track marine Sr. Given that the Vetreny Belt epidote reflects ~90 % marine Sr, the 2.41 Ga hydrothermal system reflects interaction between basalt and seawater with Ca and SO_4 concentrations ranging between 30-40 and 0-10 mM, respectively. These values represent the original marine input and the effects of phase separation.
5. Considering the global Sr budget, periods of high oceanic Ca/SO_4 were likely accompanied by an increased fraction of marine Sr permanently stored in insoluble silicates within altered oceanic crust. While some fraction of marine Sr returns into the ocean upon dissolution of anhydrite during periods of low Ca/SO_4, insoluble silicates provided a long-term sink for Sr that was subsequently subducted.

6. ACKNOWLEDGEMENTS

We dedicate this paper to Vyacheslav Stepanovich Kulikov, who contributed fundamentally to the studies of stratigraphy, petrology, geochemistry and metallogeny of Precambrian formations on the Baltic Shield, including the Vetreny Belt. This work was supported by the National Geographic Young Explorer Grant (CP-079ER-17), Evolving Earth Grant (2017) to DZ and National Science Foundation grant EAR-1447337 to INB. We thank Igor Puchtel and Sophia Mezhelovskaya for providing the samples of fresh komatiitic basalts from the Lava Lake locality (Victoria lake, near Levgora, Russia; Fig. 4) and the samples of the carbonates from the underlying Kozhozero suite. We also thank Matvey Debolsky and Alan Rempel for the discussions of the dual-porosity model. We are grateful to Torsten Vennemann for running the carbonate samples for conventional C- and O-isotope values. We appreciate the thoughtful

reviews by Michael Antonelli and 3 anonymous reviewers. Michelle Foley is thanked for proofreading the manuscript with a fresh pair of eyes.

7. REFERENCES

Alexander R. J., Harper G. D. and Bowman J. R. (1993) Oceanic faulting and fault-controlled subseafloor hydrothermal alteration in the sheeted dike complex of the Josephine Ophiolite. *J. Geophys. Res.* **98**, 9731.

Alt J. C. and Bach W. (2006) Oxygen isotope composition of a section of lower oceanic crust, ODP Hole 735B: OXYGEN ISOTOPE COMPOSITION OF CRUST. *Geochem. Geophys. Geosyst.* **7**, n/a-n/a.

Alt J. C., Davidson G. J., Teagle D. A. H. and Karson J. A. (2003) Isotopic composition of gypsum in the Macquarie Island ophiolite: Implications for the sulfur cycle and the subsurface biosphere in oceanic crust. *Geology* **31**, 549–552.

Alt J. C. and Teagle D. A. H. (2000) Hydrothermal alteration and fluid fluxes in ophiolites and oceanic crust. In *Ophiolites and oceanic crust: new insights from field studies and the Ocean Drilling Program* Geological Society of America. Available at: https://pubs.geoscienceworld.org/books/book/501/chapter/3800685 [Accessed February 17, 2020].

Alt J. C., Teagle D. a H., Bach W., Halliday A. N. and Erzinger J. (1996) Stable and strontium isotopic profiles through hydrothermally altered upper oceanic crust, Hole 504B. *Proceedings of the Ocean Drilling Program Scientific Results* **148**, 57–69.

Alt, Kinoshita H., Stokking L. B. and Michael P. J. eds. (1996) *Proceedings of the Ocean Drilling Program, 148 Scientific Results.*, Ocean Drilling Program. Available at: http://www-odp.tamu.edu/publications/148_SR/148TOC.HTM [Accessed February 17, 2020].

Antonelli M. A., Pester N. J., Brown S. T. and DePaolo D. J. (2017) Effect of paleoseawater composition on hydrothermal exchange in midocean ridges. *Proc Natl Acad Sci USA* **114**, 12413–12418.

Bach W. and Humphris S. E. (1999) Relationship between the Sr and O isotope compositions of hydrothermal fluids and the spreading and magma-supply rates at oceanic spreading centers. *Geology* **27**, 1067–1070.

Becker K. (1985) Large-scale electrical resistivity and bulk porosity of the oceanic crust, Deep Sea Drilling Project Hole 504B, Costa Rica Rift. In *Initial reports DSDP, Leg 83, Balboa to Balboa, Panama* US Govt. Printing Office; UK distributors, IPOD Committee, NERC, Swindon. pp. 419–427.

Bekker A., Kaufman A. J., Karhu J. A., Beukes N. J., Swart Q. D., Coetzee L. L. and Eriksson K. A. (2001) Chemostratigraphy of the Paleoproterozoic Duitschland Formation, South Africa: implications for coupled climate change and carbon cycling. *American Journal of Science* **301**, 261–285.

Bekker A., Krapež B. and Karhu J. A. (2020) Correlation of the stratigraphic cover of the Pilbara and Kaapvaal cratons recording the lead up to Paleoproterozoic Icehouse and the GOE. *Earth-Science Reviews* **211**, 103389.

Bekker A., Sial A. N., Karhu J. A., Ferreira V. P., Noce C. M., Kaufman A. J., Romano A. W. and Pimentel M. M. (2003) Chemostratigraphy of carbonates from the Minas Supergroup, Quadrilátero Ferryífero (Iron Quadrangle), Brazil: A stratigraphic record of early proterozoic atmospheric, biogeochemical and climactic change. *American Journal of Science* **303**, 865–904.

Berndt M. E., Seyfried Jr W. E. and Janecky D. R. (1989) Plagioclase and epidote buffering of cation ratios in mid-ocean ridge hydrothermal fluids: Experimental results in and near the supercritical region. *Geochimica et Cosmochimica Acta* **53**, 2283–2300.

Berner E. K. and Berner R. A. (1996) Global environment water, air, and geochemical cycles Prentice-Hall. *Englewood Cliffs, NewJersey*.

Berner R. A. (2004) A model for calcium, magnesium and sulfate in seawater over Phanerozoic time. *American Journal of Science* **304**, 438–453.

Bickle M. J. and Teagle D. A. H. (1992) Strontium alteration in the Troodos ophiolite: implications for fluid fluxes and geochemical transport in mid-ocean ridge hydrothermal systems. *Earth and Planetary Science Letters* **113**, 219–237.

Bindeman I. N., Zakharov D. O., Palandri J., Greber N. D., Dauphas N., Retallack G. J., Hofmann A., Lackey J. S. and Bekker A. (2018) Rapid emergence of subaerial landmasses and onset of a modern hydrologic cycle 2.5 billion years ago. *Nature* **557**, 545–548.

Blanc G., Boulegue J. and Michard A. (1995) Isotope compositions of the Red Sea hydrothermal end-member. *Comptes rendus de l'Académie des sciences. Série 2. Sciences de la terre et des planètes* **320**, 1187–1193.

Blättler C. L., Bergmann K. D., Kah L. C., Gómez-Pérez I. and Higgins J. A. (2020) Constraints on Meso-to Neoproterozoic seawater from ancient evaporite deposits. *Earth and Planetary Science Letters* **532**, 115951.

Broecker W. S. and Peng T. H. (1982) Tracers in the Sea, 690 pp. *Lamont-Doherty Geological Observatory, Palisades, NY*.

Brown S. T., Kennedy B. M., DePaolo D. J., Hurwitz S. and Evans W. C. (2013) Ca, Sr, O and D isotope approach to defining the chemical evolution of hydrothermal fluids: Example from Long Valley, CA, USA. *Geochimica et Cosmochimica Acta* **122**, 209–225.

Brown S. T., Turchyn A. V., Bickle M. J., Davis A. C., Alt J. C., Bédard J. H., Skulski T. and DePaolo D. J. (2020) High-temperature kinetic isotope fractionation of calcium in epidosites from modern and ancient seafloor hydrothermal systems. *Earth and Planetary Science Letters* **535**, 116101.

Butterfield D. A., Massoth G. J., McDuff R. E., Lupton J. E. and Lilley M. D. (1990) Geochemistry of hydrothermal fluids from Axial Seamount hydrothermal emissions study vent field, Juan de Fuca Ridge: Subseafloor boiling and subsequent fluid-rock interaction. *Journal of Geophysical Research: Solid Earth* **95**, 12895–12921.

927 Canfield D. E. (1998) A new model for Proterozoic ocean chemistry. *Nature* **396**, 450–453.

928 Canfield D. E. and Farquhar J. (2009) Animal evolution, bioturbation, and the sulfate
929 concentration of the oceans. *Proceedings of the National Academy of Sciences* **106**,
930 8123–8127.

931 Cano E. J., Sharp Z. D. and Shearer C. K. (2020) Distinct oxygen isotope compositions of the
932 Earth and Moon. *Nature Geoscience*, 1–5.

933 Coggon R. M., Teagle D. A. H., Smith-Duque C. E., Alt J. C. and Cooper M. J. (2010)
934 Reconstructing Past Seawater Mg/Ca and Sr/Ca from Mid-Ocean Ridge Flank Calcium
935 Carbonate Veins. *Science* **327**, 1114–1117.

936 Coogan L. A. (2009) Altered oceanic crust as an inorganic record of paleoseawater Sr
937 concentration. *Geochemistry, Geophysics, Geosystems* **10**.

938 Craig H. (1966) Isotopic Composition and Origin of the Red Sea and Salton Sea Geothermal
939 Brines. *Science* **154**, 1544–1548.

940 Crockford P. W., Kunzmann M., Bekker A., Hayles J., Bao H., Halverson G. P., Peng Y., Bui T.
941 H., Cox G. M., Gibson T. M., Wörndle S., Rainbird R., Lepland A., Swanson-Hysell N.
942 L., Master S., Sreenivas B., Kuznetsov A., Krupenik V. and Wing B. A. (2019) Claypool
943 continued: Extending the isotopic record of sedimentary sulfate. *Chemical Geology* **513**,
944 200–225.

945 Crowe S. A., Paris G., Katsev S., Jones C., Kim S.-T., Zerkle A. L., Nomosatryo S., Fowle D.
946 A., Adkins J. F. and Sessions A. L. (2014) Sulfate was a trace constituent of Archean
947 seawater. *Science* **346**, 735–739.

948 De Hoog J. C. M., Taylor B. E. and Van Bergen M. J. (2001) Sulfur isotope systematics of
949 basaltic lavas from Indonesia: implications for the sulfur cycle in subduction zones. *Earth*
950 *and Planetary Science Letters* **189**, 237–252.

951 De Ronde C. E. J., Channer D. M. deR., Faure K., Bray C. J. and Spooner E. T. C. (1997) Fluid
952 chemistry of Archean seafloor hydrothermal vents: Implications for the composition of
953 circa 3.2 Ga seawater. *Geochimica et Cosmochimica Acta* **61**, 4025–4042.

954 DePaolo D. J. (2006) Isotopic effects in fracture-dominated reactive fluid–rock systems.
955 *Geochimica et Cosmochimica Acta* **70**, 1077–1096.

956 DePaolo D. J. and Getty S. R. (1996) Models of isotopic exchange in reactive fluid-rock
957 systems: Implications for geochronology in metamorphic rocks. *Geochimica et*
958 *Cosmochimica Acta* **60**, 3933–3947.

959 Eiler J. M., Schiano P., Kitchen N. and Stolper E. M. (2000) Oxygen-isotope evidence for
960 recycled crust in the sources of mid-ocean-ridge basalts. *Nature* **403**, 530–534.

961 Evans K. A., Tomkins A. G., Cliff J. and Fiorentini M. L. (2014) Insights into subduction zone
962 sulfur recycling from isotopic analysis of eclogite-hosted sulfides. *Chemical Geology*
963 **365**, 1–19.

964 Fakhraee M., Hancisse O., Canfield D. E., Crowe S. A. and Katsev S. (2019) Proterozoic
965 seawater sulfate scarcity and the evolution of ocean–atmosphere chemistry. *Nature*
966 *Geoscience* **12**, 375–380.

967 Farquhar J. and Wing B. A. (2003) Multiple sulfur isotopes and the evolution of the atmosphere.
968 *Earth and Planetary Science Letters* **213**, 1–13.

969 Fisher A. T. (1998) Permeability within basaltic oceanic crust. *Rev. Geophys.* **36**, 143–182.

970 Flament N., Coltice N. and Rey P. F. (2008) A case for late-Archaean continental emergence
971 from thermal evolution models and hypsometry. *Earth and Planetary Science Letters*
972 **275**, 326–336.

973 Galili N., Shemesh A., Yam R., Brailovsky I., Sela-Adler M., Schuster E. M., Collom C., Bekker
974 A., Planavsky N., Macdonald F. A., and others (2019) The geologic history of seawater
975 oxygen isotopes from marine iron oxides. *Science* **365**, 469–473.

976 Gillis K. M., Coogan L. A. and Pedersen R. (2005) Strontium isotope constraints on fluid flow in
977 the upper oceanic crust at the East Pacific Rise. *Earth and Planetary Science Letters* **232**,
978 83–94.

979 Gognon, J.E., Samson, I.M., Fryer, B.J., Anderson, A.J. and Marshall, D. (2003) LA-ICP-MS
980 analysis of fluid inclusions. *Fluid inclusions Anal. Interpret. Mineral. Assoc. Canada*
981 *Short Course Notes* **32**, 291–318.

982 Guillong M., Meier D. L., Allan M. M., Heinrich C. A. and Yardley B. W. (2008) Appendix A6:
983 SILLS: A MATLAB-based program for the reduction of laser ablation ICP-MS data of
984 homogeneous materials and inclusions. *Mineralogical Association of Canada Short*
985 *Course* **40**, 328–333.

986 Gumsley A. P., Chamberlain K. R., Bleeker W., Söderlund U., de Kock M. O., Larsson E. R. and
987 Bekker A. (2017) Timing and tempo of the Great Oxidation Event. *Proceedings of the*
988 *National Academy of Sciences* **114**, 1811–1816.

989 Habicht K. S., Gade M., Thamdrup B., Berg P. and Canfield D. E. (2002) Calibration of sulfate
990 levels in the Archean ocean. *Science* **298**, 2372–2374.

991 Halevy I., Peters S. E. and Fischer W. W. (2012) Sulfate burial constraints on the Phanerozoic
992 sulfur cycle. *Science* **337**, 331–334.

993 Halverson G. P., Dudás F. Ö., Maloof A. C. and Bowring S. A. (2007) Evolution of the
994 87Sr/86Sr composition of Neoproterozoic seawater. *Palaeogeography,*
995 *Palaeoclimatology, Palaeoecology* **256**, 103–129.

996 Halverson G. P. and Hurtgen M. T. (2007) Ediacaran growth of the marine sulfate reservoir.
997 *Earth and Planetary Science Letters* **263**, 32–44.

998 Hanski E. J. and Melezhik V. A. (2013) 3.2 Litho- and Chronostratigraphy of the
999 Palaeoproterozoic Karelian Formations. In *Reading the Archive of Earth's Oxygenation:*
1000 *Volume 1: The Palaeoproterozoic of Fennoscandia as Context for the Fennoscandian*
1001 *Arctic Russia - Drilling Early Earth Project* (eds. Victor A. Melezhik, A. R. Prave, A. E.
1002 Fallick, L. R. Kump, H. Strauss, A. Lepland, and Eero J. Hanski). Frontiers in Earth
1003 Sciences. Springer, Berlin, Heidelberg. pp. 39–110. Available at:
1004 https://doi.org/10.1007/978-3-642-29682-6_4 [Accessed December 1, 2020].

1005 Harris M., Coggon R. M., Smith-duque C. E., Cooper M. J., Milton J. A. and Teagle D. A. H.
1006 (2015) Channelling of hydrothermal fluids during the accretion and evolution of the

upper oceanic crust : Sr isotope evidence from ODP Hole 1256D. *Earth and Planetary Science Letters* **416**, 56–66.

Hayba D. O. and Ingebritsen S. E. (1997) Multiphase groundwater flow near cooling plutons. *J. Geophys. Res.* **102**, 12235–12252.

Hayles J., Gao C., Cao X., Liu Y. and Bao H. (2018) Theoretical calibration of the triple oxygen isotope thermometer. *Geochimica et Cosmochimica Acta* **235**, 237–245.

Heinrich C. A., Pettke T., Halter W. E., Aigner-Torres M., Audétat A., Günther D., Hattendorf B., Bleiner D., Guillong M. and Horn I. (2003) Quantitative multi-element analysis of minerals, fluid and melt inclusions by laser-ablation inductively-coupled-plasma mass-spectrometry. *Geochimica et Cosmochimica Acta* **67**, 3473–3497.

Hodell D. A., Mead G. A. and Mueller P. A. (1990) Variation in the strontium isotopic composition of seawater (8 Ma to present): Implications for chemical weathering rates and dissolved fluxes to the oceans. *Chemical Geology: Isotope Geoscience section* **80**, 291–307.

Holland H. D. (1984) *The chemical evolution of the atmosphere and oceans*., Princeton University Press.

Jaffrés J. B. D., Shields G. A. and Wallmann K. (2007) The oxygen isotope evolution of seawater: A critical review of a long-standing controversy and an improved geological water cycle model for the past 3.4 billion years. *Earth-Science Reviews* **83**, 83–122.

Jamieson J. W., Wing B. A., Farquhar J. and Hannington M. D. (2013) Neoarchaean seawater sulphate concentrations from sulphur isotopes in massive sulphide ore. *Nature Geoscience* **6**, 61–64.

Jochum K. P., Weis U., Stoll B., Kuzmin D., Yang Q., Raczek I., Jacob D. E., Stracke A., Birbaum K. and Frick D. A. (2011) Determination of reference values for NIST SRM 610–617 glasses following ISO guidelines. *Geostandards and Geoanalytical Research* **35**, 397–429.

Kadko D., Gronvold K. and Butterfield D. (2007) Application of radium isotopes to determine crustal residence times of hydrothermal fluids from two sites on the Reykjanes Peninsula, Iceland. *Geochimica et Cosmochimica Acta* **71**, 6019–6029.

Kadko D. and Moore W. (1988) Radiochemical constraints on the crustal residence time of submarine hydrothermal fluids: Endeavour Ridge. *Geochimica et Cosmochimica Acta* **52**, 659–668.

Kah L. C., Lyons T. W. and Frank T. D. (2004) Low marine sulphate and protracted oxygenation of the Proterozoic biosphere. *Nature* **431**, 834–838.

Kawahata H., Kusakabe M. and Kikuchi Y. (1987) Strontium, oxygen, and hydrogen isotope geochemistry of hydrothermally altered and weathered rocks in DSDP Hole 504B, Costa Rica Rift. *Earth and Planetary Science Letters* **85**, 343–355.

Knauth P. L. (2005) Temperature and salinity history of the Precambrian ocean: implications for the course of microbial evolution. *Palaeogeography, Palaeoclimatology, Palaeoecology* **219**, 53–69.

Kulikov V. S., Bychkova Y. V., Kulikova V. V. and Ernst R. (2010) The Vetreny Poyas (Windy Belt) subprovince of southeastern Fennoscandia: An essential component of the ca. 2.5–2.4 Ga Sumian large igneous provinces. *Precambrian Research* **183**, 589–601.

Kulikov V. S., Bychkova Y. V., Kulikova V. V., Kostitsyn Y. A., Pokrovsky O. S. and Vasil'ev M. V. (2008) The Ruiga intrusion: A typical example of a shallow-facies paleoproterozoic peridotite-gabbro-komatiite-basaltic association of the Vetreny Belt, Southeastern Fennoscandia. *Petrology* **16**, 531–551.

Kump L. R. (1989) Alternative modeling approaches to the geochemical cycles of carbon, sulfur, and strontium isotopes. *American Journal of Science* **289**, 390–410.

Kump L. R. and Seyfried W. E. (2005) Hydrothermal Fe fluxes during the Precambrian: Effect of low oceanic sulfate concentrations and low hydrostatic pressure on the composition of black smokers. *Earth and Planetary Science Letters* **235**, 654–662.

Kuznetsov A. B., Melezhik V. A., Gorokhov I. M., Melnikov N. N., Konstantinova G. V., Kutyavin E. P. and Turchenko T. L. (2010) Sr isotopic composition of Paleoproterozoic 13C-rich carbonate rocks: The Tulomozero Formation, SE Fennoscandian Shield. *Precambrian Research* **182**, 300–312.

Lowenstein T. K., Hardie L. A., Timofeeff M. N. and Demicco R. V. (2003) Secular variation in seawater chemistry and the origin of calcium chloride basinal brines. *Geology* **31**, 857–860.

Matsuhisa Y., Goldsmith J. R. and Clayton R. N. (1978) Mechanisms of hydrothermal crystallization of quartz at 250°C and 15 kbar. *Geochimica et Cosmochimica Acta* **42**, 173–182.

Matthews A., Goldsmith J. R. and Clayton R. N. (1983) Oxygen isotope fractionation between zoisite and water. *Geochimica et Cosmochimica Acta* **47**, 645–654.

McCulloch M. T., Gregory R. T., Wasserburg G. J. and Taylor H. P. (1981) Sm-Nd, Rb-Sr, and ^{18}O/^{16}O isotopic systematics in an oceanic crustal section: Evidence from the Samail Ophiolite. *J. Geophys. Res.* **86**, 2721–2735.

Mezhelovskaya S. V., Korsakov A. K., Mezhelovskii A. D. and Bibikova E. V. (2016) Age range of formation of sedimentary-volcanogenic complex of the Vetreny Belt (the southeast of the Baltic Shield). *Stratigraphy and Geological Correlation* **24**, 105–117.

Miller M. F., Pack A., Bindeman I. N. and Greenwood R. C. (2020) Standardizing the reporting of Δ\textsuperscript$\prime$17O data from high precision oxygen triple-isotope ratio measurements of silicate rocks and minerals. *Chemical Geology* **532**, 119332.

Mills R. A., Teagle D. A. H. and Tivey M. K. (1998) 10. FLUID MIXING AND ANHYDRITE PRECIPITATION WITHIN THE TAG MOUND1. In *Proceedings of the ocean drilling program: Scientific results* The Program. p. 119.

Norton D. (1978) Sourcelines, sourceregions, and pathlines for fluids in hydrothermal systems related to cooling plutons. *Economic Geology* **73**, 21–28.

Ojakangas R. W., Marmo J. S. and Heiskanen K. I. (2001) Basin evolution of the Paleoproterozoic Karelian Supergroup of the Fennoscandian (Baltic) Shield. *Sedimentary Geology* **141–142**, 255–285.

O'Neil J. R., Clayton R. N. and Mayeda T. K. (1969) Oxygen isotope fractionation in divalent metal carbonates. *The Journal of Chemical Physics* **51**, 5547–5558.

Pack A. and Herwartz D. (2014) The triple oxygen isotope composition of the Earth mantle and understanding ΔO17 variations in terrestrial rocks and minerals. *Earth and Planetary Science Letters* **390**, 138–145.

Pack A., Tanaka R., Hering M., Sengupta S., Peters S. and Nakamura E. (2016) The oxygen isotope composition of San Carlos olivine on the VSMOW2-SLAP2 scale: San Carlos olivine on the VSMOW2-SLAP2 scale. *Rapid Commun. Mass Spectrom.* **30**, 1495–1504.

Palmer M. R. and Edmond J. M. (1989) The strontium isotope budget of the modern ocean. *Earth and Planetary Science Letters* **92**, 11–26.

Pettke T., Oberli F., Audétat A., Guillong M., Simon A. C., Hanley J. J. and Klemm L. M. (2012) Recent developments in element concentration and isotope ratio analysis of individual fluid inclusions by laser ablation single and multiple collector ICP-MS. *Ore Geology Reviews* **44**, 10–38.

Planavsky N. J., Bekker A., Hofmann A., Owens J. D. and Lyons T. W. (2012) Sulfur record of rising and falling marine oxygen and sulfate levels during the Lomagundi event. *Proceedings of the National Academy of Sciences* **109**, 18300–18305.

Prokoph A., Shields G. A. and Veizer J. (2008) Compilation and time-series analysis of a marine carbonate δ18O, δ13C, 87Sr/86Sr and δ34S database through Earth history. *Earth-Science Reviews* **87**, 113–133.

Puchtel I., Brügmann G., Hofmann A., Kulikov V. and Kulikova V. (2001) Os isotope systematics of komatiitic basalts from the Vetreny belt, Baltic Shield: evidence for a chondritic source of the 2.45 Ga plume. *Contributions to Mineralogy and Petrology* **140**, 588–599.

Puchtel I. S., Haase K. M., Hofmann A. W., Chauvel C., Kulikov V. S., Garbe-Schönberg C.-D. and Nemchin A. A. (1997) Petrology and geochemistry of crustally contaminated komatiitic basalts from the Vetreny Belt, southeastern Baltic Shield: evidence for an early Proterozoic mantle plume beneath rifted Archean continental lithosphere. *Geochimica et Cosmochimica Acta* **61**, 1205–1222.

Puchtel I. S., Hofmann A. W., Mezger K., Shchipansky A. A., Kulikov V. S. and Kulikova V. V. (1996) Petrology of a 2.41 Ga remarkably fresh komatiitic basalt lava lake in Lion Hills, central Vetreny Belt, Baltic Shield. *Contributions to Mineralogy and Petrology* **124**, 273–290.

Puchtel I. S., Touboul M., Blichert-Toft J., Walker R. J., Brandon A. D., Nicklas R. W., Kulikov V. S. and Samsonov A. V. (2016) Lithophile and siderophile element systematics of Earth's mantle at the Archean–Proterozoic boundary: evidence from 2.4 Ga komatiites. *Geochimica et Cosmochimica Acta* **180**, 227–255.

Reed M. H., Spycher N. F. and Palandri J. (2010) Users Guide for CHIM-XPT: A Program for Computing Reaction Processes in Aquous-Mineral Gas Systems and MINITAB Guide. *Eugene, OR: University of Oregon*.

Ryb U. and Eiler J. M. (2018) Oxygen isotope composition of the Phanerozoic ocean and a possible solution to the dolomite problem. *Proc Natl Acad Sci USA* **115**, 6602–6607.

Satkoski A. M., Lowe D. R., Beard B. L., Coleman M. L. and Johnson C. M. (2016) A high continental weathering flux into Paleoarchean seawater revealed by strontium isotope analysis of 3.26 Ga barite. *Earth and Planetary Science Letters* **454**, 28–35.

Schlöglova K., Wälle M. and Heinrich C. A. (2017) LA-ICP-MS analysis of fluid inclusions: contamination effects challenging micro-analysis of elements close to their detection limit. *Journal of analytical atomic spectrometry* **32**, 1052–1063.

Schröder S., Bekker A., Beukes N. J., Strauss H. and Niekerk H. S. V. (2008) Rise in seawater sulphate concentration associated with the Paleoproterozoic positive carbon isotope excursion: evidence from sulphate evaporites in the ∼2.2–2.1 Gyr shallow-marine Lucknow Formation, South Africa. *Terra Nova* **20**, 108–117.

Scott C., Lyons T. W., Bekker A., Shen Y., Poulton S. W., Chu X. and Anbar A. D. (2008) Tracing the stepwise oxygenation of the Proterozoic ocean. *Nature* **452**, 456–459.

Scott C., Wing B. A., Bekker A., Planavsky N. J., Medvedev P., Bates S. M., Yun M. and Lyons T. W. (2014) Pyrite multiple-sulfur isotope evidence for rapid expansion and contraction of the early Paleoproterozoic seawater sulfate reservoir. *Earth and Planetary Science Letters* **389**, 95–104.

Seo J. H., Guillong M., Aerts M., Zajacz Z. and Heinrich C. A. (2011) Microanalysis of S, Cl, and Br in fluid inclusions by LA–ICP-MS. *Chemical Geology* **284**, 35–44.

Sharp Z. D., Wostbrock J. A. G. and Pack A. (2018) Mass-dependent triple oxygen isotope variations in terrestrial materials. *Geochem. Persp. Let.*, 27–31.

Sheldon N. D. (2006) Precambrian paleosols and atmospheric CO2 levels. *Precambrian Research* **147**, 148–155.

Shields G. and Veizer J. (2002) Precambrian marine carbonate isotope database: Version 1.1: CARBONATE ISOTOPE DATABASE. *Geochem.-Geophys.-Geosyst.* **3**, 1 of 12–12 12.

Spötl C. and Vennemann T. W. (2003) Continuous-flow isotope ratio mass spectrometric analysis of carbonate minerals. *Rapid Communications in Mass Spectrometry* **17**, 1004–1006.

Syverson D. D., Scheuermann P., Higgins J. A., Pester N. J. and Seyfried Jr W. E. (2018) Experimental partitioning of Ca isotopes and Sr into anhydrite: Consequences for the cycling of Ca and Sr in subseafloor mid-ocean ridge hydrothermal systems. *Geochimica et Cosmochimica Acta* **236**, 160–178.

Teagle D. A.H., Alt J. C., Chiba H. and Halliday A. N. (1998) Dissecting an active hydrothermal deposit: the strontium and oxygen isotopic anatomy of the TAG hydrothermal mound - anhydrite. *Proceedings of the Ocean Drilling Program: Scientific Results* **158**, 129–141.

Teagle D. A. H., Alt J. C. and Halliday A. N. (1998) Tracing the evolution of hydrothermal fluids in the upper oceanic crust: Sr-isotopic constraints from DSDP/ODP Holes 504B and 896A. *Geological Society, London, Special Publications* **148**, 81–97.

Tostevin R., Turchyn A. V., Farquhar J., Johnston D. T., Eldridge D. L., Bishop J. K. and McIlvin M. (2014) Multiple sulfur isotope constraints on the modern sulfur cycle. *Earth and planetary science letters* **396**, 14–21.

Turchyn A. V., Alt J. C., Brown S. T., DePaolo D. J., Coggon R. M., Chi G., Bédard J. H. and Skulski T. (2013) Reconstructing the oxygen isotope composition of late Cambrian and Cretaceous hydrothermal vent fluid. *Geochimica et Cosmochimica Acta* **123**, 440–458.

Turchyn A. V. and DePaolo D. J. (2019) Seawater Chemistry Through Phanerozoic Time. *Annual Review of Earth and Planetary Sciences* **47**, 197–224.

Turner E. C. and Bekker A. (2016) Thick sulfate evaporite accumulations marking a mid-Neoproterozoic oxygenation event (Ten Stone Formation, Northwest Territories, Canada). *Bulletin* **128**, 203–222.

Warke M. R., Rocco T. D., Zerkle A. L., Lepland A., Prave A. R., Martin A. P., Ueno Y., Condon D. J. and Claire M. W. (2020) The Great Oxidation Event preceded a Paleoproterozoic "snowball Earth." *PNAS* **117**, 13314–13320.

Wood J. R. and Hewett T. A. (1982) Fluid convection and mass transfer in porous sandstones—A theoretical model. *Geochimica et Cosmochimica Acta* **46**, 1707–1713.

Young G. M. (2013) Precambrian supercontinents, glaciations, atmospheric oxygenation, metazoan evolution and an impact that may have changed the second half of Earth history. *Geoscience Frontiers* **4**, 247–261.

Zachos J., Pagani M., Sloan L., Thomas E. and Billups K. (2001) Trends, rhythms, and aberrations in global climate 65 Ma to present. *science* **292**, 686–693.

Zakharov D. O. and Bindeman I. N. (2019) Triple oxygen and hydrogen isotopic study of hydrothermally altered rocks from the 2.43–2.41 Ga Vetreny belt, Russia: An insight into the early Paleoproterozoic seawater. *Geochimica et Cosmochimica Acta* **248**, 185–209.

Zakharov D. O., Bindeman I. N., Serebryakov N. S., Prave A. R., Azimov P. Y. and Babarina I. I. (2019a) Low δ18O rocks in the Belomorian belt, NW Russia, and Scourie dikes, NW Scotland: A record of ancient meteoric water captured by the early Paleoproterozoic global mafic magmatism. *Precambrian Research* **333**, 105431.

Zakharov D. O., Bindeman I. N., Tanaka R., Friðleifsson G. Ó., Reed M. H. and Hampton R. L. (2019b) Triple oxygen isotope systematics as a tracer of fluids in the crust: A study from modern geothermal systems of Iceland. *Chemical Geology* **530**, 119312.

Zakharov D. O., Marin-Carbonne J., Alleon J. and Bindeman I. N. (2021) Triple Oxygen Isotope Trend Recorded by Precambrian Cherts: A Perspective from Combined Bulk and in situ Secondary Ion Probe Measurements. *Reviews in Mineralogy and Geochemistry* **86**, 323–365.

Zhang S., Zhou R. and DePaolo D. J. (2020) The seawater Sr/Ca ratio in the past 50 Myr from bulk carbonate sediments corrected for diagenesis. *Earth and Planetary Science Letters* **530**, 115949.

Zheng Y.-F. (1993) Calculation of oxygen isotope fractionation in hydroxyl-bearing silicates. *Earth and Planetary Science Letters* **120**, 247–263.

In Press:

Herwartz, D., 2021. Triple oxygen isotope variations in Earth's crust. Reviews in Mineralogy and Geochemistry 86, 291-322.

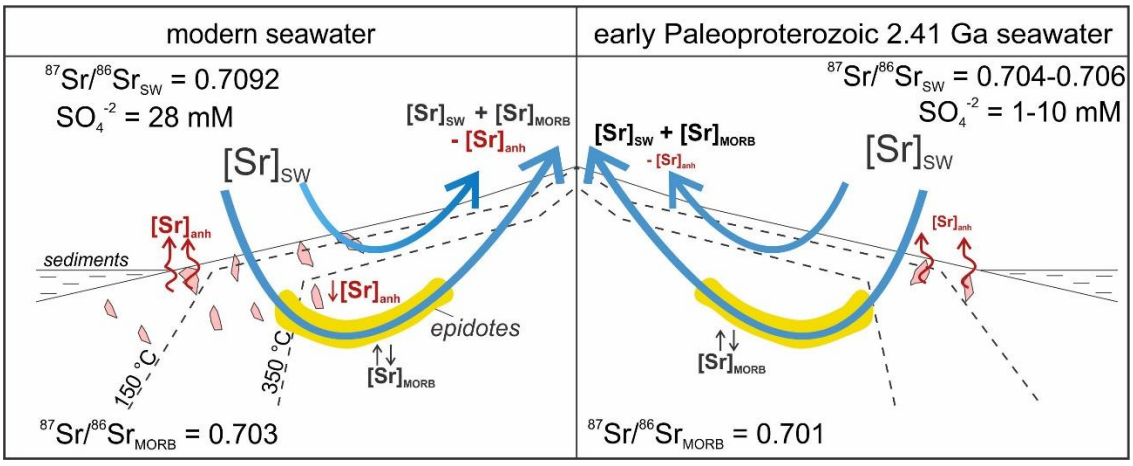

Figure 1. Schematic illustration of Sr distribution in oceanic crust resulted from seawater-basalt reaction and anhydrite precipitation at mid-ocean ridges in modern (left) and the envisioned low-sulfate early Paleoproterozoic 2.41 Ga oceans (right). Precipitation of sulfate (shown with red-pink shapes) in modern and Phanerozoic hydrothermal systems removes marine Sr (shown as $[Sr]_{sw}$) from the fluids proportional to the amount of anhydrite-hosted $[Sr]_{anh}$. Since the early Paleoproterozoic (2.43-2.41 Ga) marine sulfate was likely low, the hydrothermal systems of the 2.41 Ga Vetreny Belt were precipitating less anhydrite compared to modern systems. Thus, we envision that a higher fraction of $[Sr]_{SW}$ was able to reach Ca-silicates of high-temperature altered oceanic crust such as epidote.

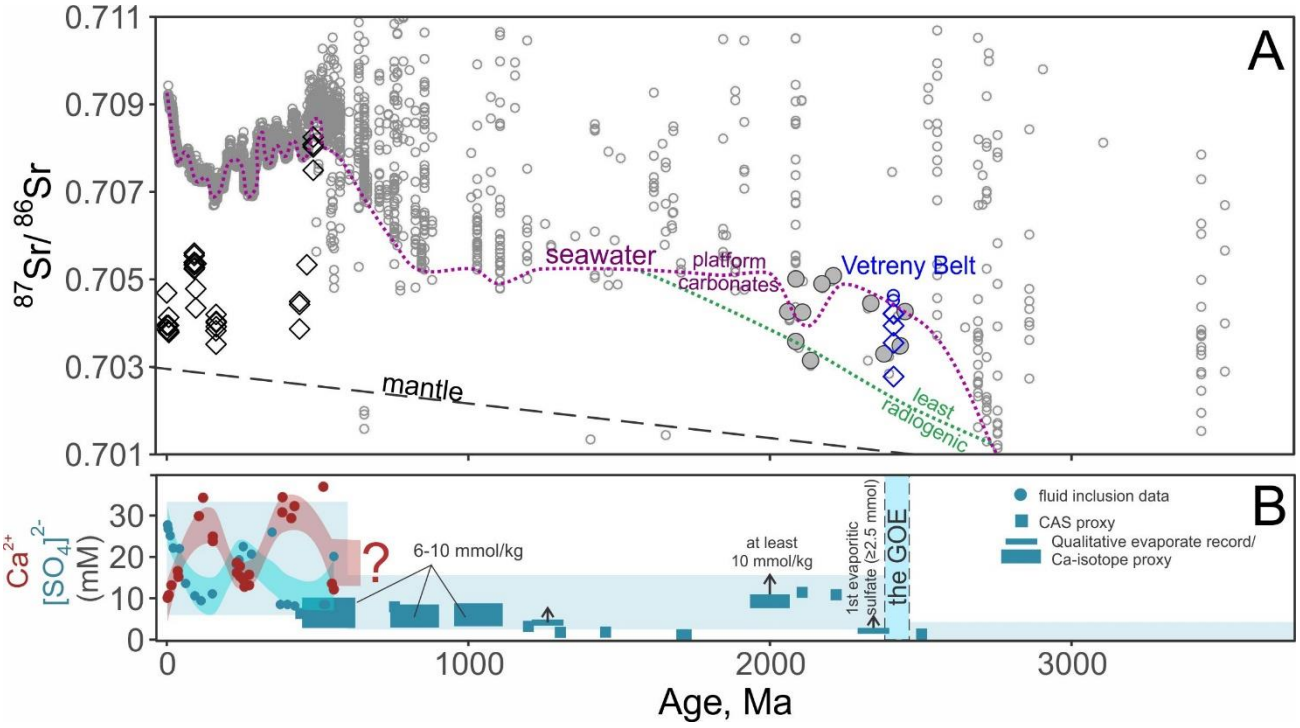

Figure 2. **A** – Strontium isotope evolution of seawater as reflected by carbonates (grey open circles; compiled from (Shields and Veizer, 2002; Prokoph et al., 2008). The early Paleoproterozoic seawater curve between 2.5 and 2.0 Ga is reconstructed from the least radiogenic samples (green dotted line Shields and Veizer, 2002) and from platform carbonates shown as the grey filled circles (Kuznetsov et al., 2010 and references therein). Oceanic epidotes (open diamonds) plot between the mantle and seawater values at respective geologic times depicting the relative contributions of marine vs basaltic Sr. The Vetreny Belt epidotes and carbonates are shown with blue diamonds and circles respectively. **B** – Marine sulfate and calcium levels over the geologic history as reconstructed in previous studies from fluid inclusion data, carbonate-associated sulfate (CAS), occurrences of evaporitic sulfate and associated Ca-isotope fractionation (Lowenstein et al., 2003; Kah et al., 2004; Canfield and Farquhar, 2009; Planavsky et al., 2012; Schröder et al., 2008; Blättler et al., 2020, 2018).

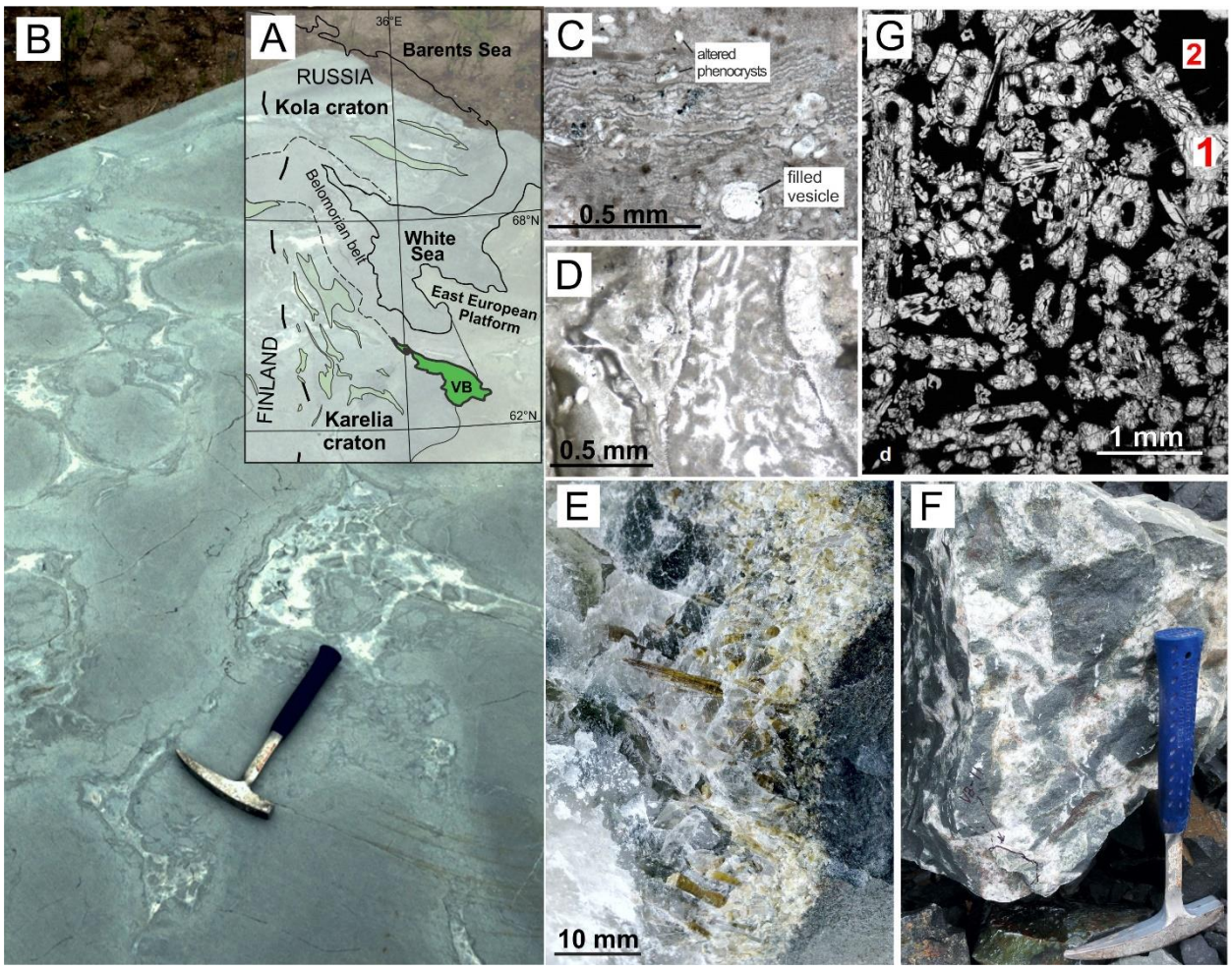

Figure 3. A – Schematic map of the Baltic Shield showing the location of the Vetreny Belt (VB) within the Karelia craton. Archean greenstone belts are shown in pale green. **B** – Hydrothermally altered pillow basalt section exposed by a circular saw cut (locality Myandukha). The length of the hammer is about 30 cm for scale. **C** – Altered basaltic lava with glass hydration texture shown in crossed polarized light. A filled vesicle and altered phenocrysts are visible. **D** – Altered pillow rind with remnants of glassy shard texture. **E** – Quartz-epidote-calcite vein used for this study (sample VB8A). **F** – Brecciated basaltic dike cemented with quartz-epidote aggregate. **G** – Unaltered komatiitic basalt with olivine phenocrysts (marked 1 in red) and pristine fresh volcanic glass (marked 2) as seen in cross polarized light (photo adapted from Puchtel et al., 1996).

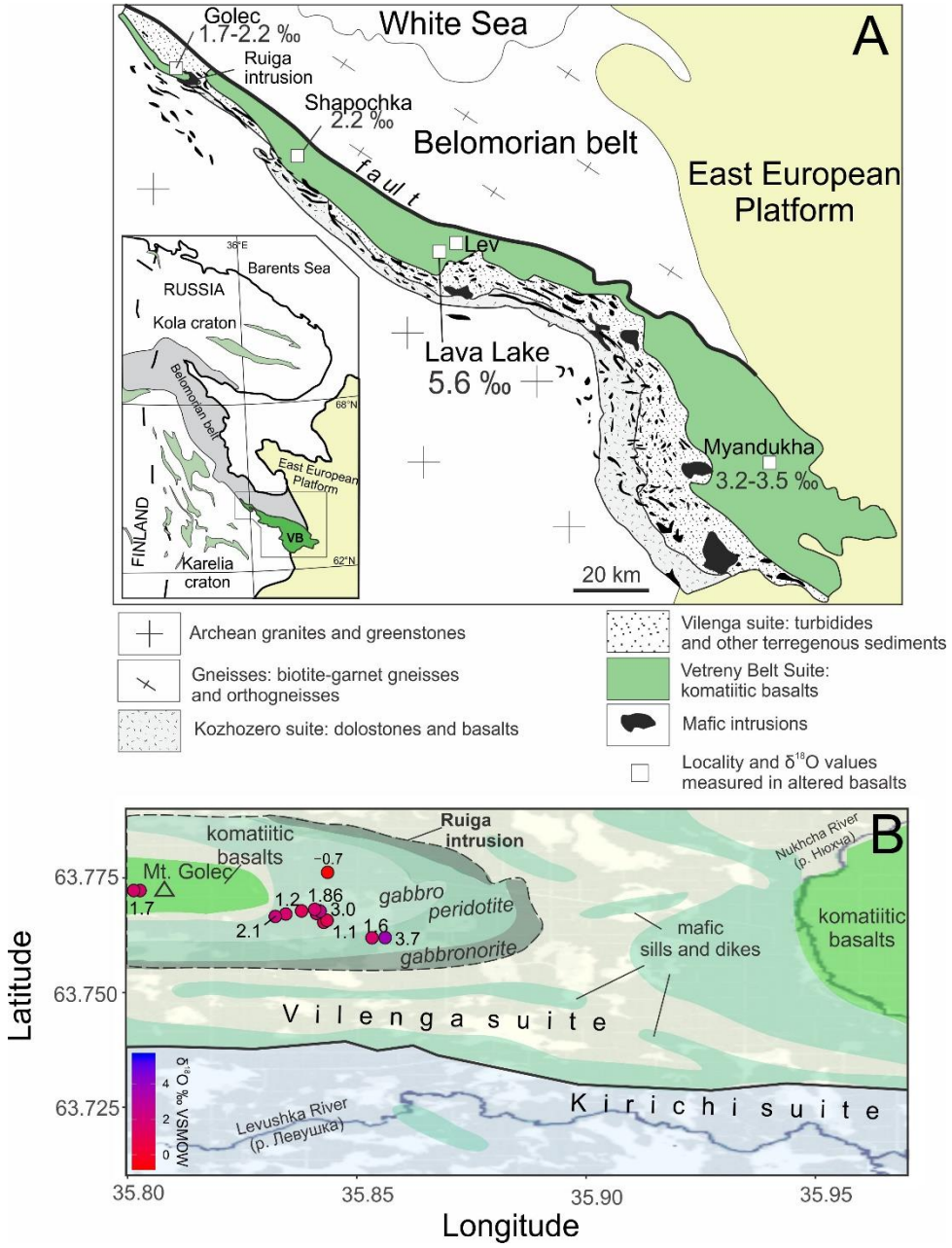

Figure 4. A schematic geological map of the Vetreny Belt (**A**) and the vicinity of Ruiga intrusion (**B;** modified from Kulikov et al., 2008) along with our $\delta^{18}O$ sampling of altered gabbroids and komatiitic basalts (values from here and Zakharov and Bindeman, 2019).

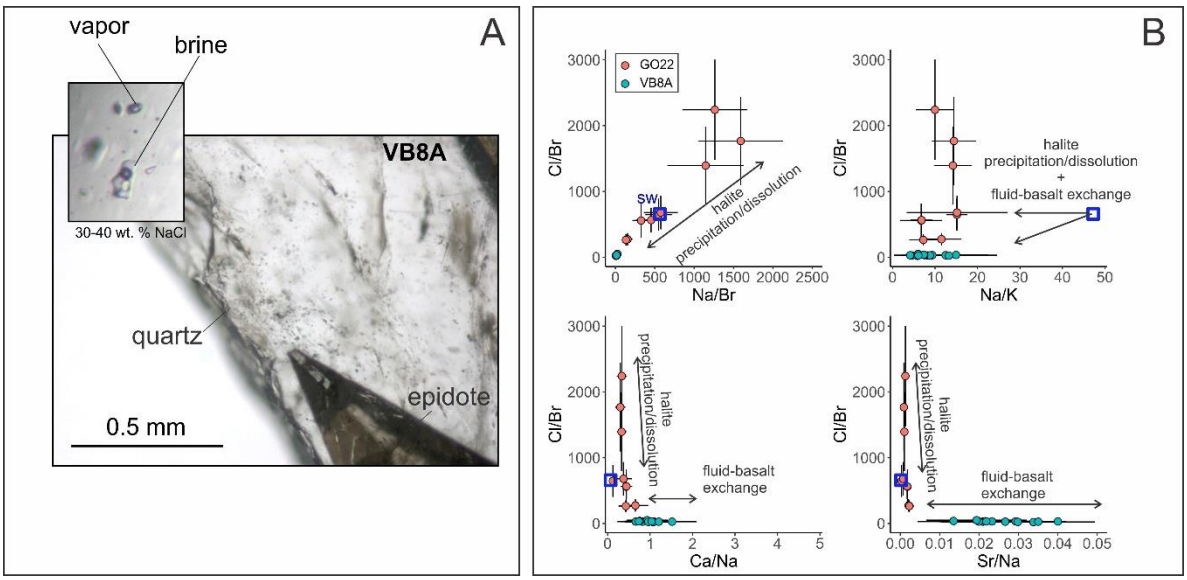

Figure 5. A – The photograph of sample VB8A featuring quartz hosting numerous fluid inclusions and an epidote crystal (labeled). The inset shows a high-salinity fluid inclusion (labeled "brine") that homogenizes to liquid and a vapor-dominated fluid inclusion that homogenizes to vapor (labeled "vapor"). Presence of both types of inclusions indicates that the fluid was undergoing phase separation. **B** – The elemental ratios of fluid inclusions determined by LA-ICP-MS. The Cl/Br and Na/Br ratios are sensitive to precipitation or dissolution of halite, while Na/K, Ca/Na and Sr/Na also reflect the extent of seawater-basalt exchange. The modern seawater composition is shown with a blue square in each panel. We interpret the change in ratios in GO22 fluid inclusions chiefly as a result of halite-precipitation and dissolution yet moderate fluid-basalt exchange. Meanwhile, the VB8A ratios indicate halite precipitation and also, likely, its fractionation from the remaining fluid and subsequent phase-separation. In addition, elemental ratios measured in VB8A inclusions appear to be more modified due to fluid-basalt exchange compared to the GO22 inclusions.

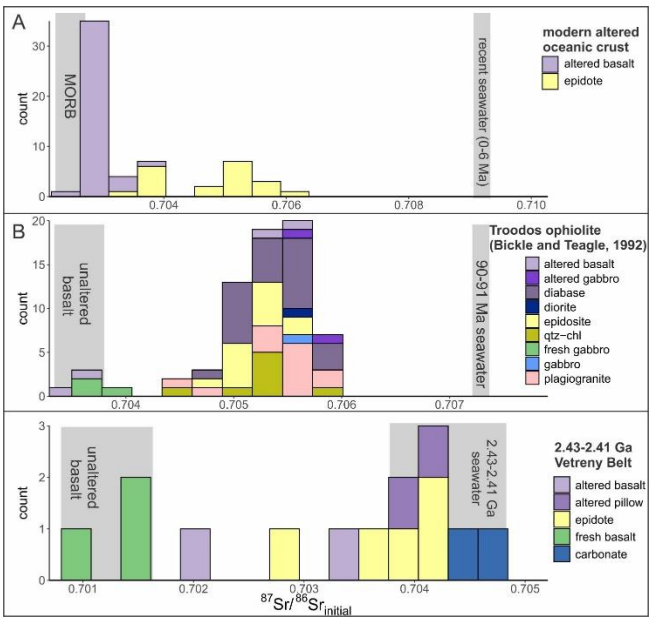

Figure 6. A – Stacked histograms of Sr isotope values measured in epidotes and altered basalts from modern oceanic crust (**A**; this study and from Kawahata et al., 1987; Alt et al., 1996; Harris et al., 2015), Troodos ophiolite (**B**; Bickle and Teagle, 1992; quartz-chlorite aggregates abbreviated to qtz-chl) and the Vetreny Belt (**C;** this study). Note the difference in the horizontal scale as it is adjusted so that the contemporaneous seawater and unaltered basalt (shown as mid-ocean ridge basalt, or MORB, for modern samples) are aligned for convenient comparison. The $^{87}Sr/^{86}Sr$ of the 2.43-2.41 Ga seawater is poorly constrained and thus, is shown with a wider range of values, encompassing contemporaneous carbonates (e.g. Kuznetsov et al., 2010) and the carbonates from the underlying Kozhozero suite. Fresh komatiitic basalts sampled at the lava lake from the Vetreny Belt represent the value of unaltered basalt.

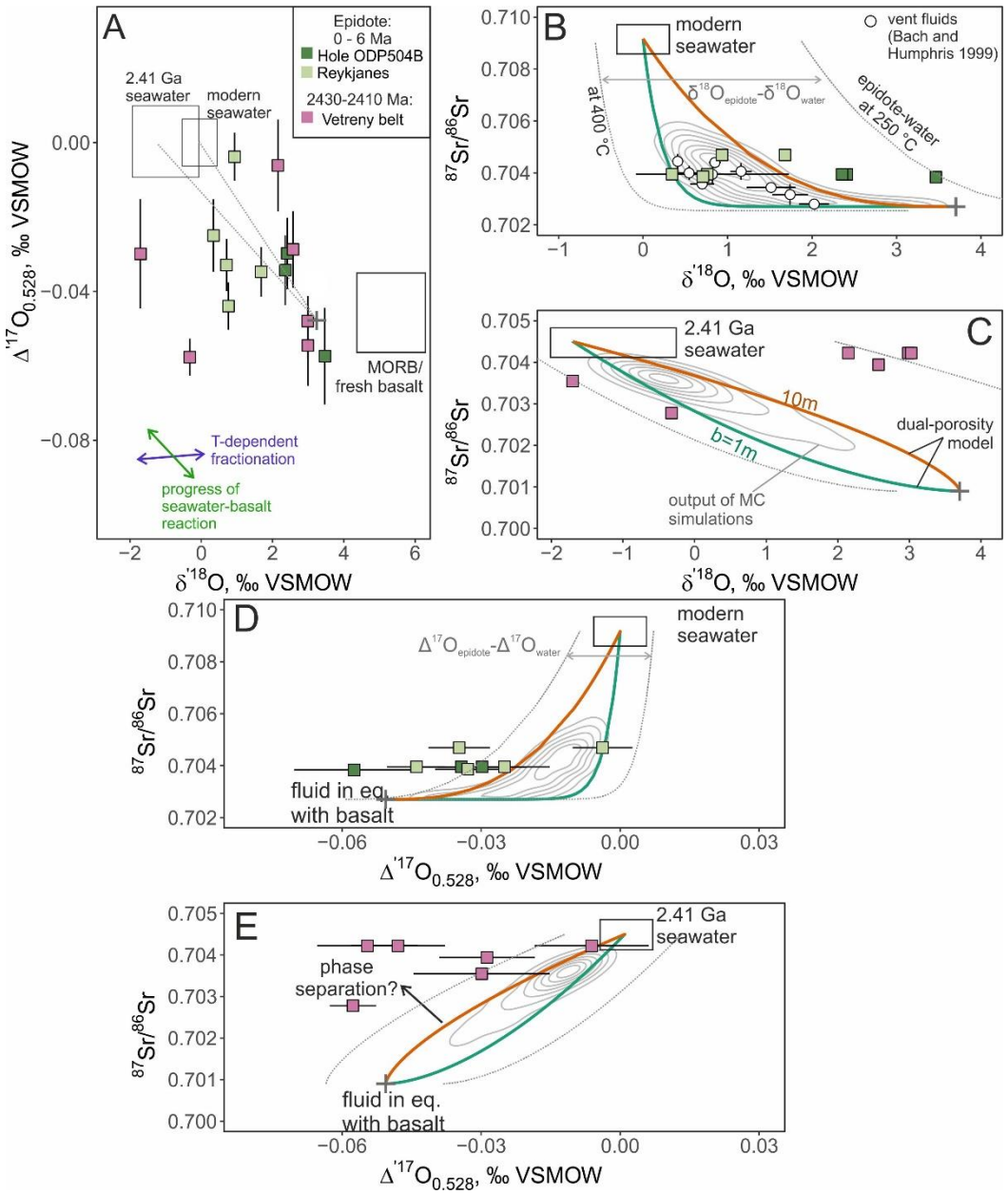

Figure 7. A - The $\delta'^{18}O$-$\Delta'^{17}O$ coordinates show that modern oceanic epidotes plot in the region between the seawater values and fluids fully exchanged with mid-ocean ridge basalt (MORB). The linearized notation $\delta'^{18}O = 10^3\ln(1+\delta^{18}O/1000)$ is adopted. The Vetreny Belt epidotes plot in the same region deviating towards slightly lower $\delta^{18}O$ fluids suggesting seawater of around -2 ‰. The fresh unaltered basalt values are shown with the box and the corresponding high-temperature equilibrium fluid is shown with a cross. **B** – Modern oceanic epidotes and fluids (fluid values are from Bach and Humphris, 1999) plotted in $\delta'^{18}O$-$^{87}Sr/^{86}Sr$ coordinates. Dual-porosity model outputs with different fracture spacings are shown with green and orange lines (1 and 10 m, respectively). The system's Sr_{rock}/Sr_{fluid} ratio is 16 defined by modern-day concentrations of seawater and MORB. **C** – The Vetreny Belt epidote plotted in the same coordinates, with the dual-porosity model shown for a system in which the concentration ratio $Sr_{rock}/Sr_{fluid} = 1$. The grey-concentric region shows the output of the Monte-Carlo (MC)

simulations. The dotted lines show the limits of the equilibrium epidote compositions, i.e. $\delta^{18}O_{epidote}$-$\delta^{18}O_{water}$ and envisioned $\Delta^{17}O_{epidote}$-$\Delta^{17}O_{water}$, based on the temperature range 250-400 °C (fractionation factor for $^{18}O/^{16}O$ from Zheng, 1993). The error bars denote single grain analyses with 1 standard error. The vent fluids plotted with bars denoting the range of values reported in (Bach and Humphris, 1999). **D** and **E** – Modern and ancient epidote samples are plotted in $\Delta'^{17}O$ – $^{87}Sr/^{86}Sr$ coordinates.

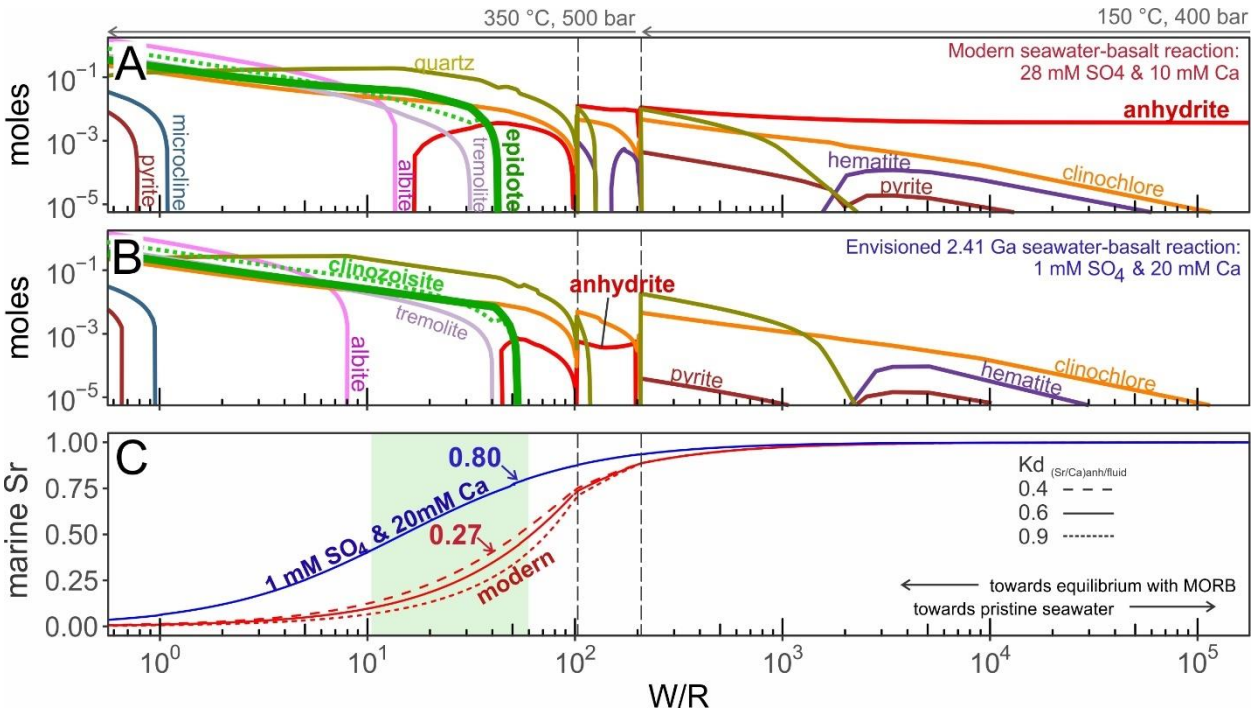

Figure 8. Selected equilibrium mineral assemblages shown as a function of as seawater-basalt reaction at different water/rock (W/R) mass ratios. The calculation is carried out using the program CHIM-XPT (Reed et al., 2010) following the procedure outlined in Section 2.5 (*first set*). The modern seawater-basalt reaction is shown in panel (**A**) yielding an abundance of anhydrite around 10^{-2} moles at high W/R. The low sulfate seawater-basalt reaction as envisioned at 2.41 Ga (**B**) exhibits considerably lower concentrations of equilibrium anhydrite (~10^{-3} moles) at limited W/R of around 35-110. The vertical dashed lines indicate W/R ratios where fractionation of minerals from fluid was invoked in the calculation. **C** – Corresponding Sr-isotope shifts calculated using the Sr-Ca-partition coefficient in anhydrite K_D (see Eqs. 3 and 4). The isotope ratio is shown as the fraction of marine Sr, i.e. [$^{87}Sr/^{86}Sr_{fluid}$ - $^{87}Sr/^{86}Sr_{basalt}$]/[$^{87}Sr/^{86}Sr_{sw}$ - $^{87}Sr/^{86}Sr_{basalt}$]. The $^{87}Sr/^{86}Sr_{SW}$ = 1 denoting Sr-isotope composition of pristine seawater.

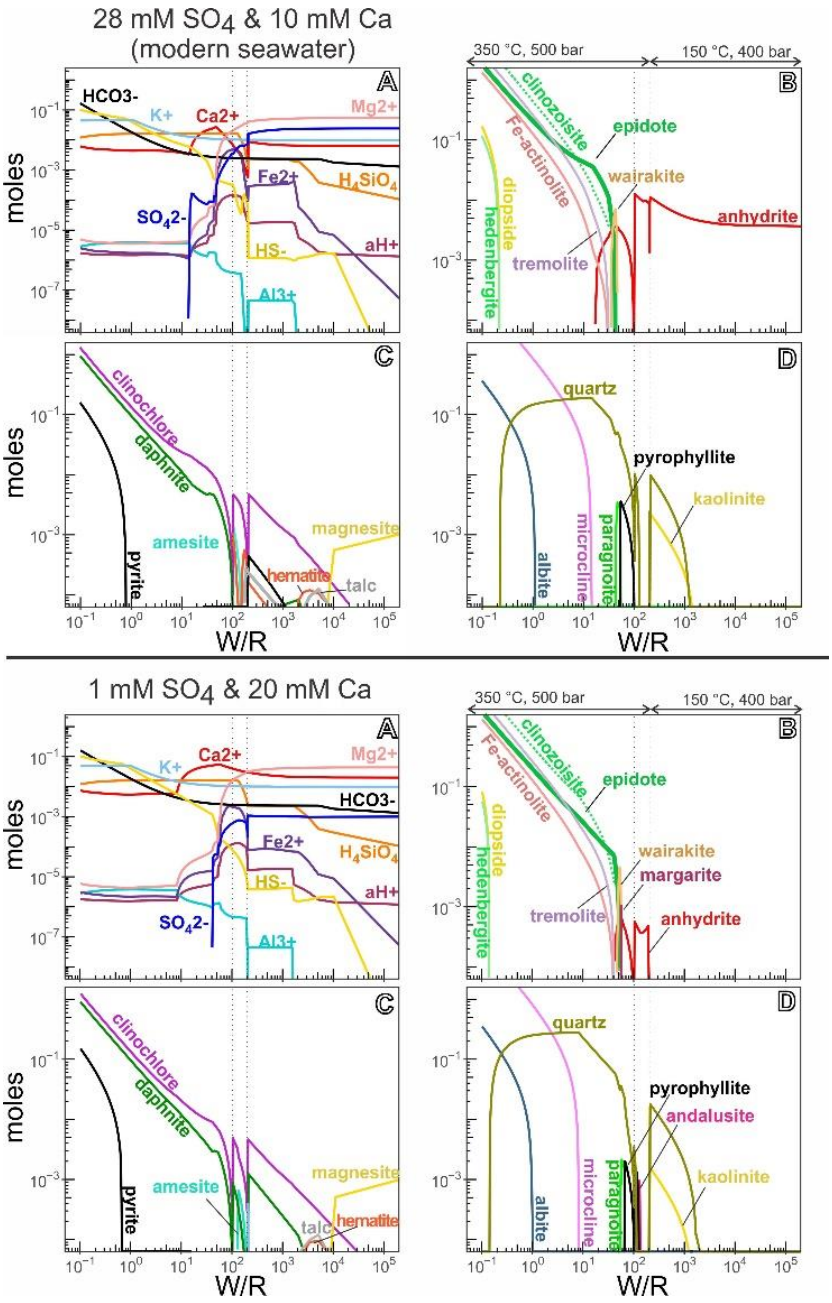

Figure 9. Result of the seawater-basalt equilibrium reaction calculations shown in Figure 8 with the complete list of aqueous and mineral species including their solid solutions. Total molalities of aqueous component species are shown in panels **A** with the exception of sodium and chlorine that stay almost unchanged. **B** – molar abundances of Ca-bearing minerals, including anhydrite and epidote. **C** - molar abundance of equilibrium Fe/Mg-bearing minerals from the same calculation. **D** - Molar abundance of equilibrium alumosilicate minerals and quartz in the same calculation.

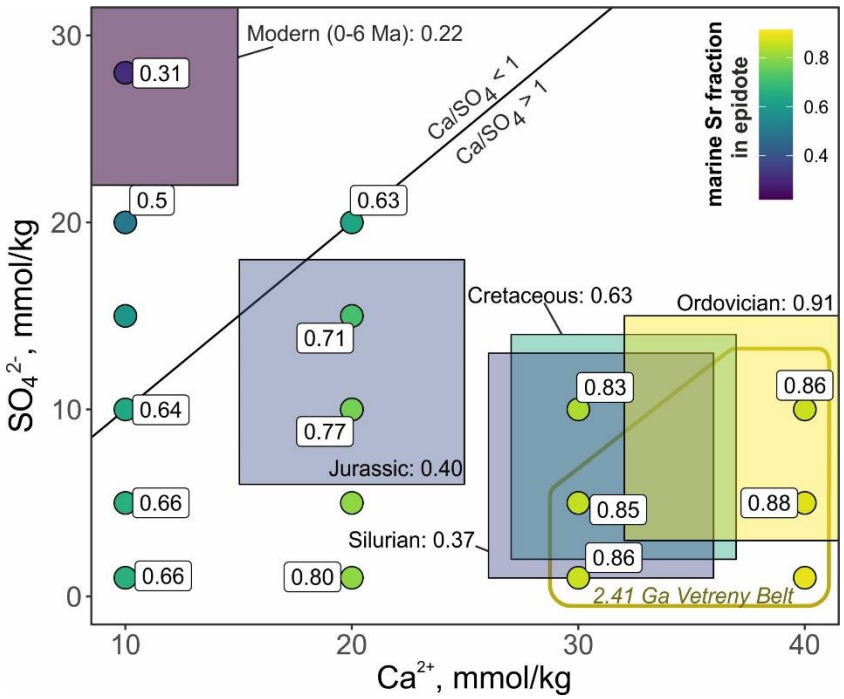

Figure 10. The outputs of seawater-basalt reaction calculations plotted as a function of marine Ca and SO_4 concentrations. Each color-coded point represents the $^{87}Sr/^{86}Sr$ value of epidote produced in our calculations relative to the initial seawater value (pure seawater $^{87}Sr/^{86}Sr = 1$). Some points are labeled with numbers representing the fraction of marine Sr. The solid black line depicts seawater composition with $Ca/SO_4 = 1$. The large squares represent the estimated Ca and SO_4 concentrations of Phanerozoic seawater, color-coded by the $^{87}Sr/^{86}Sr$ values of oceanic epidotes from contemporaneous ophiolites (see Fig. 2 and references within the caption). The highest fraction of marine Sr measured in epidote from Phanerozoic ophiolites is indicated (e.g. 91% in an Ordovician ophiolite; Turchyn et al., 2013). The Vetreny Belt epidote records ~90 % marine Sr (shown as outlined field) and is most consistent with a very high Ca/SO_4 ratio of the 2.41 Ga seawater.

1375 **Table 1.** Ranges of values used in the Monte Carlo simulation of dual porosity model

Variable	Minimum	Maximum	Units	Sources
b, fracture spacing	1	10	m	DePaolo, 2006
R, dissolution-precipitation rate	0.00005	0.0002	g g^{-1} $year^{-1}$	DePaolo, 2006; Kadko et al., 2007
v_f, fluid velocity	1	100	m yr^{-1}	Hayba and Ingebritsen, 1997
ϕ, matrix porosity	0.01	0.02	none	Becker, 1985

1376

1377 **Table 2.** Molal concentrations of solutes in initial seawater and weight percent oxides of basaltic
1378 rock used in the mineral-aqueous equilibrium calculations.

Ion	Concentration in modern seawater (mmol/kg)	Envisioned 2.43-2.41 Ga seawater	Initial basalt composition expressed in	Weight %
Cl^-	550	604*		
SO_4^{2-}	28	1	H_2O	0.21
HCO_3^-	2.3	-	CO_2	0.70
HS^-	$3.0 \cdot 10^{-8}$	-	FeS	0.30
H_4SiO_4	0.11	-	SiO_2	50.49
Al^{3+}	$3.0 \cdot 10^{-3}$	-	Al_2O_3	15.48
Ca^{2+}	10	20	CaO	11.52
Mg^{2+}	55	45	MgO	7.84
Fe^{2+}	$5.4 \cdot 10^{-3}$	-	FeO/Fe_2O_3	7.98/1.25
K^+	10	-	K_2O	0.18
Na^+	469	-	Na_2O	2.70
Sr^{2+}	$87 \cdot 10^{-3}$	$160 \cdot 10^{-3}$	Sr	200 ppm

1379 * - chlorinity of seawater was adjusted to maintain neutral charge balance

1380

1381

1382

1383

1384

1385

Table 3. Results of the fluid inclusion LA-ICP-MS measurements reported as ratios relative to Na concentration. The number of fluid inclusions within each measured assemblage is shown as # FI. Only samples with signals above detection limits are shown.

Sample	# FI	Li/Na	B/Na	Mg/Na	Al/Na	Cl/Na	K/Na	Ca/Na	Mn/Na	Fe/Na	Cu/Na	Zn/Na	Br/Na	Rb/Na	Sr/Na	Cs/Na	Ba/Na	Pb/Na
GO22-1	3		0.0017	0.0028		1.91	0.18	0.43	0.0027	0.042	0.0047			0.00031	0.0027	0.00007	0.0034	
GO22-1	3		0.0048	0.0004	0.0044	1.82	0.11	0.21	0.0015		0.0032		0.0063	0.00014	0.0013	0.00004	0.0020	0.00005
GO22-2	3		0.0030	0.0003		1.82	0.11	0.65	0.0013	0.013	0.0039	0.0008	0.0060	0.00013	0.0027	0.00003	0.0038	0.00018
GO22-2	6	0.0010	0.0021	0.0068	0.1506	1.72	0.12	0.52	0.0034	0.022	0.0074		0.0022	0.00018	0.0035	0.00005	0.0100	0.00012
GO22-2	4	0.0017	0.0028	0.0011	0.0635	1.88	0.12	0.57	0.0047	0.025	0.0098	0.0048	0.0030	0.00018	0.0040	0.00002	0.0115	0.00024
GO22-2	4		0.0038	0.0010	0.0706	2.74	0.17	0.58	0.0046	0.030	0.0077		0.0028	0.00024	0.0049	0.00005	0.0148	0.00011
GO22-3	3		0.0044	0.0016	0.0020	2.75	0.15	1.14	0.0092	0.023	0.0126		0.0224	0.00035	0.0081		0.0121	
GO22-3	3	0.0014	0.0042	0.0010	0.0010	2.64	0.25	0.76	0.0119	0.044	0.0138	0.0003	0.0106	0.00035	0.0069	0.00003	0.0323	0.00018
GO22-3	5	0.0047	0.0039	0.0009	0.0277	3.05	0.23	0.75	0.0162	0.050	0.0072		0.0259	0.00023	0.0087		0.0409	0.00088
GO22-3	4	0.0034	0.0040	0.0033	0.2203	1.92	0.25	0.77	0.0153	0.067	0.0078	0.0031	0.0076	0.00032	0.0066		0.0452	0.00121
VB8A-chip2-1	2	0.0009	0.0060	0.0022	0.0076	3.44	0.18	1.89	0.2056	0.247		0.0593	0.2358	0.00010	0.0887	0.00023	0.1474	0.05665
VB8A-chip2-1	6	0.0013	0.0021	0.0039	0.0136	4.11	0.21	1.43	0.1136	0.119		0.0423	0.3190	0.00046	0.0800	0.00039	0.1171	0.03927
VB8A-chip2-1	4		0.0056			3.46	0.11	1.30	0.1346	0.078		0.0405	0.2141	0.00026	0.0824	0.00038	0.1300	0.03667
VB8A-chip2-1	3	0.0005	0.0053			3.18	0.19	1.15	0.1621	0.174	0.0002	0.0315	0.2372	0.00049	0.0761	0.00038	0.0785	0.04671
VB8A-chip2-2	4			0.0067		3.40	0.23	1.31	0.1868	0.209		0.0445	0.2243	0.00059	0.1116	0.00052	0.1316	0.03338
VB8A-chip2-2	3		0.0091			6.02	0.37	2.65	0.1494	0.196		0.0427	0.4696	0.00187	0.1016	0.00103	0.1918	0.05110
VB8A-chip2-2	7		0.0042	0.0024	0.0046	2.79	0.23	1.32	0.0768	0.107		0.0214	0.1585	0.00069	0.0516	0.00034	0.0893	0.02019
VB8A-chip2-2	4	0.0067	0.0044	0.0054	0.0038	3.09	0.28	1.62	0.0898	0.110	0.0010	0.0229	0.1341	0.00078	0.0739	0.00037	0.0792	0.02199
VB8A-chip2-3	5		0.0048			3.14	0.14	1.28	0.1125	0.099		0.0357	0.2150	0.00040	0.0833	0.00040	0.1122	0.02913
VB8A-chip2-3	4		0.0051	0.0017	0.0099	3.56	0.13	1.67	0.1396	0.140	0.0011	0.0428	0.3146	0.00063	0.1138	0.00048	0.1463	0.04091
VB8A-chip2-3	3	0.0027	0.0020			3.97	0.29	1.87	0.1629	0.284		0.0587	0.4004	0.00149	0.1289	0.00053	0.1606	0.06562
VB8A-chip3	3	0.0426	0.0074			4.12	0.28	2.10	0.1973	0.166		0.0536	0.3229	0.00145	0.1335	0.00073	0.1710	0.05080
VB8A-chip3	2	0.0159	0.0032	0.0051		3.46	0.41	1.80	0.2687	0.279		0.0519	0.2450	0.00133	0.1526	0.00077	0.2726	0.04762

Table 4. Results of the fluid inclusion LA-ICP-MS measurements reported as concentrations in μg/g calculated based on the average salinity of the fluid inclusions measured in each sample.

Sample	# FI	Li	B	Na	Mg	Al	Cl	Br	K	Ca	Mn	Fe	Cu	Zn	Br	Rb	Sr	Cs	Ba	Pb
GO22-1	3		202	118163	328		225763	0	21703	50828	317	4987	560			36	315	7.9	406	
GO22-1	3		639	132169	52	582	240900	837	14836	28325	194		419		837	19	167	4.9	266	6.5
GO22-2	3		350	118280	36		215276	712	13260	76672	152	1553	465	100	712	15	324	3.6	451	21
GO22-2	6	116	248	118607	808	17865	203494	259	13950	61797	409	2588	874		259	22	412	6.5	1191	14
GO22-2	4	187	310	110728	119	7035	208034	336	13253	63295	520	2752	1089	531	336	20	441	2.6	1270	26
GO22-2	4		413	109135	113	7705	298996	300	18580	63438	501	3250	845		300	26	537	5.1	1610	12
GO22-3	3		399	90430	140	180	248253	2030	13364	103041	835	2087	1140		2030	32	729		1096	
GO22-3	3	135	410	97271	100	99	256936	1033	24546	73886	1153	4300	1340	32	1033	34	670	2.7	3138	17
GO22-3	5	537	449	114205	107	3159	348855	2958	26771	85421	1856	5678	817		2958	26	996		4674	101
GO22-3	4	331	385	97317	325	21441	186946	744	24230	75180	1492	6561	760	302	744	31	645		4402	118
VB8A-chip2-1	2	52	361	60394	130	460	207918	14241	10983	114214	12415	14903		3581	14241	6	5357	14	8902	3421
VB8A-chip2-1	6	97	153	73142	288	996	300839	23336	15052	104458	8310	8733		3096	23336	34	5853	29	8568	2872
VB8A-chip2-1	4		437	78048			270096	16712	8882	101551	10503	6091		3158	16712	21	6429	30	10149	2862
VB8A-chip2-1	3	42	409	76754			244461	18207	14819	88446	12438	13356	18	2419	18207	38	5840	29	6025	3585
VB8A-chip2-2	4			72370	484		245955	16236	16492	94693	13519	15143		3219	16236	43	8077	38	9524	2416
VB8A-chip2-2	3		462	50978			307021	23939	18956	134867	7614	10011		2179	23939	95	5181	52	9779	2605
VB8A-chip2-2	7		324	76597	181	351	213893	12141	17747	100736	5885	8176		1642	12141	53	3952	26	6839	1546
VB8A-chip2-2	4	485	319	71840	387	271	222330	9632	20360	116479	6454	7910	71	1648	9632	56	5306	26	5690	1580
VB8A-chip2-3	5		417	86570			271896	18609	11785	110829	9737	8535		3091	18609	35	7211	34	9710	2522
VB8A-chip2-3	4		380	75028	128	741	266756	23601	9616	125195	10476	10507	82	3211	23601	47	8537	36	10974	3070
VB8A-chip2-3	3	190	141	70152			278367	28090	20363	131198	11426	19926		4116	28090	104	9043	37	11270	4603
VB8A-chip3	3	2712	473	63598			262249	20537	17785	133525	12548	10556		3409	20537	92	8492	47	10874	3231
VB8A-chip3	2	1011	203	63405	324		219532	15537	25973	114396	17040	17676		3290	15537	85	9674	49	17284	3019

Table 5. Strontium isotope data for the modern oceanic epidotes and the Vetreny Belt rocks.

Sample	Description	Rb, ppm	Sr, ppm	Rb/Sr	$^{87}Sr/^{86}Sr$ measured	$^{87}Sr/^{86}Sr_{initial}$		± 1se
Vetreny Belt rocks								
						at 2.41 Ga	at 2.43 Ga	
12106	fresh basalt	24.3	390	0.062	0.70783	0.70155		0.00069
12124	fresh basalt	15.9	224	0.071	0.70868	0.70152		0.00071
12101	fresh basalt	15.9	259	0.061	0.70705	0.70086		0.00069
Altered basalt lithologies								
VB16	altered pillow rind	bdl[1]	17	<0.059	0.70428			
VB16 duplicate	altered pillow rind				0.70423			
VB25	altered basalt	7.4	250	0.030	0.70643	0.70345		0.00029
VB9	altered pillow rind	1.6	50	0.032	0.70739	0.70416		0.00033
My1	altered basalt (hyaloclastite)	4.3	231	0.019	0.70603	0.70416		0.00020
GO25	altered basalt	15.2	297	0.051	0.70803	0.70287		0.00069
Epidote separates								
GO22	epidote	bdl	1053	<0.001	0.70360	0.70360		0.00003
GO4	epidote	bdl	2350	<0.001	0.70288	0.70288		0.00003
VB24	epidote	bdl	627	<0.001	0.70394	0.70394		0.00003
VB8A	epidote	bdl	2862	<0.001	0.70423	0.70422		0.00003
Carbonates from underlying Kozhozero suite								
02-08-04	carbonate	10.7	665	0.016	0.70625	0.70463	0.70462	0.00016
02-08-03	carbonate	1.9	342	0.006	0.70510	0.70454	0.70453	0.00004
Modern oceanic epidotes from Reykjanes drilling wells (RN12 and 17B), and from Ocean Drilling Project Site 504B (Leg 83)								
						at 0-6 Ma		
RN12 1070	epidote	bdl	921	<0.001	0.704691	0.70469		0.00003
RN17B 2805.5	epidote	bdl	729	<0.001	0.703859	0.70386		0.00003
RN17B 2899.75	epidote	bdl	617	<0.001	0.703953	0.70395		0.00003
83-90R_148-149	epidote	bdl	1060	<0.001	0.703834	0.70383		0.00003
83-90R_71-72	epidote	bdl	247	<0.001	0.70395	0.70395		0.00003

1 – The Rb concentrations below the detection limit (bdl) of ~1ppm result in very low Rb/Sr ratios and negligible corrections for the $^{87}Sr/^{86}Sr_{initial}$ values (within analytical uncertainty). However, for sample VB16, the low Sr concentration results in a relatively large uncertainty of $^{87}Sr/^{86}Sr_{initial}$ (not reported).

Table 6. $\delta^{18}O$ values of unaltered komatiitic basalt from the lava lake and altered gabbros from Ruiga layered intrusion. Carbon and oxygen isotope values are provided for the carbonates of the underlying Kozhozero suite

Sample	**Material analyzed**	**$\delta^{18}O$ ‰, VSMOW**	**$\delta^{18}O$ ‰, VPDB**	**$\delta^{13}C$ ‰, VPDB**
12105*	unaltered basalt	5.6		
RU3	altered gabbro	1.1		
RU4	amphibole	1.0		
RU5	altered gabbro	1.9		
RU6	altered gabbro	3.0		
RU8	amphibole	1.2		
RU10	amphibole	2.1		
RU11	amphibole	-0.7		
S02-08-3	carbonate		-27.9	-0.95
S02-08-04	carbonate		-28.4	-1.38

* - sample from (Puchtel et al., 1996);